UNIVERSITY OF GOTHENBURG
Department of Earth Sciences
Earth Science Center

Exploring Urban Land Cover Changes and the Effect on Nocturnal Air Temperature Dynamics in Helsingborg

- A temperature modeling made with TAPM

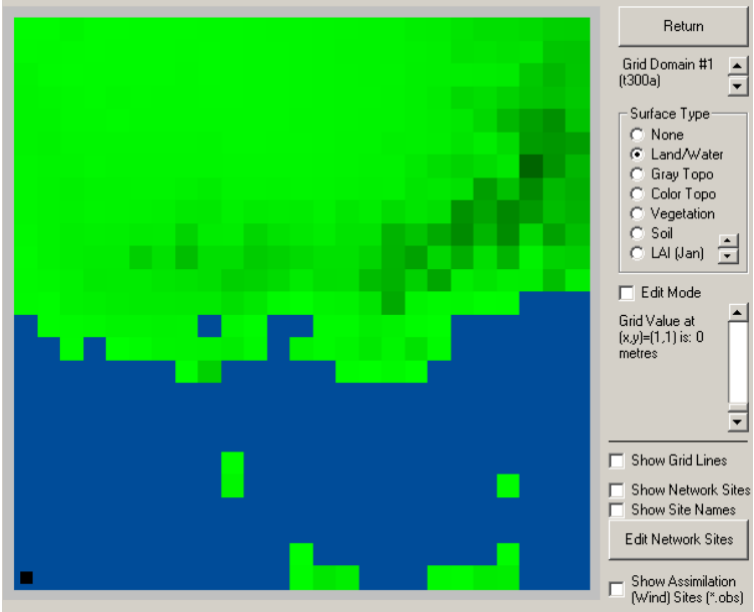

Amanda Bäck

2023

Degree of Master of Science (120 credits) with a major in Geography (30 credits), 2023

B-number	Supervisor	Examinator
B1272	Marie Haeger-Eugensson	Jacob Heyman

Abstract

In light of increasing global temperatures, urban areas face growing challenges related to heat stress. Alterations in land cover (LC) within cities contribute to changes in the intra-urban climate, predominantly driven by the replacement of vegetated surfaces with impermeable materials. These changes affect the thermal properties of urban environments, exacerbating the Urban Heat Island effect. Understanding the impact of land cover changes (LCC) on urban climate necessitates the use of remote sensing, pre-trained deep learning models, and temperature modeling techniques.

This study focuses on assessing land cover changes in the Helsingborg urban area from 2004 to 2020 through image classification utilizing a pre-trained deep learning model. Furthermore, it investigates the influence of LCC on nocturnal air temperature using the three-dimensional prognostic air pollution and meteorological model, The Air Pollution Model (TAPM). Specifically, the analysis centers around the 2018 heatwave in Sweden, aiming to evaluate TAPM's ability to differentiate between various land cover types and identify temperature patterns within the Intra-Urban Heat Islands. The deep learning model achieved an overall accuracy exceeding 90%, revealing a decline in grass surfaces and an increase in areas covered by buildings and trees. TAPM's temperature modeling, based on the land cover classifications, demonstrated distinct temperature variations at a 100 x 100-meter local scale. Additionally, it indicated a higher proportion of areas with elevated nighttime temperatures (>18°C), posing potential health risks during heatwave events akin to the summer of 2018

Key words: *Nocturnal Air Temperature, Intra-Urban Heat Island, Land Cover Classification, Deep learning, The Air Pollution Model (TAPM), Land Cover Change.*

Acknowledgments

This thesis is the outcome of a 30 credit master's thesis in Geography and was carried out during spring 2023. By completing this thesis it marks the ending of my study period and it is with mixed feelings that I leave the everyday life that has been a safe place for so many years. I would like to take this opportunity to express my gratitude for the experiences I have gained during my time at GVC. I extend my thanks to all the teachers and lectures who have played a significant role in shaping my academic journey and making it possible for me to complete my studies.

I would like to express my deepest gratitude to my supervisor Marie Haeger-Eugensson for your guidance through this demanding and stressful period. It has been a privilege to have the opportunity to learn from your extensive expertise and versatile knowledge. I would also like to thank you for granting me the opportunity to write my thesis at COWI, Gothenburg, and get to know all the talented people working there. I, especially, wanna give a huge thank you to my external supervisors, Sutthi Suteerasan and Erik Maesel from COWI. Without Sutthi's remarkable proficiency in remote sensing and image classification, or Erik's profound understanding of TAPM, I would not have been able to navigate this journey successfully. Thank you both for generously dedicating your time to answer my numerous and diverse questions, providing me with valuable insights, and offering words of encouragement.

Furthermore, I would like to extend a warm and sincere thank you to all my classmates, with whom I have had the privilege of sharing the past two years. I am confident that our paths will intersect in the professional arena, and perhaps some of us will become colleagues in the future. Regardless of the paths we choose, I wholeheartedly wish each and every one of you the very best of luck.

Amanda Bäck

Table of Contents

1. Introduction

The global human population has more than doubled since 1970, rising from 3.7 billion to 8 billion 2022 (World Population Review, n.d.). Projections from the United Nations indicate that by 2030, approximately 60% of the world's population will live in urban areas (United Nations, 2020). As cities become more densely populated and increase in size, they generate new and increased demands for housing, healthcare, energy and transportation, which often result in further land cover changes. The alterations often imply a replacement from vegetated open areas to paved surfaces and buildings. Resulting in modifications on solar radiation fluxes, the movement of water between the subsurface, and the exchange of thermal properties between the land surface and the atmosphere (Mahmood .R. et al,. 2013: Oke et al, 2017: Holmer et al, 2007: Yokobori & Ohta, 2009:Onomura et al. 2016). One of the most significant impacts of urbanization is the phenomena Urban Heat Island (UHI) and the Intra-Urban Heat Island (IUHI). UHI refers to the phenomenon of higher air temperatures in urban areas compared to their rural surroundings and IUHI occurs due to differentiations in cooling rates between various types of intra-urban sites and their intra-urban characteristics, such as, variation in vegetated surfaces, types of surface materials and building density within a urban area (Onomura et al. 2016: Hart & Sailor. 2009). The UHI and IUHI effect in mid-latitude cities becomes particularly pronounced during summer nights. This is due to the release of absorbed energy from daytime solar radiation, which prevents the ambient air temperature from decreasing. The effects caused by heat islands have been linked to a range of adverse health outcomes, including heat stress, dehydration, cardiovascular and respiratory diseases, and even mortality (Vulova,.et al. 2020).

During the summer of 2018, Sweden was affected by an extended period of extreme heat, resulting in exceptionally high temperatures nationwide (SMHI n.d.a). The Public Health Agency conducted an assessment and determined that the estimated number of additional deaths during the entire summer was approximately 650-700, in Sweden, as a result of the heat wave (Swedish Public Health Agency, 2022). Except for health related issues, summer 2018 contributed to widespread drought, leading to forest fires and water shortages (SMHI, 2018). Throughout the nation, the month of July stood out as exceptionally hot, and Helsingborg recorded its highest temperature since 1951 on July 26th, reaching a daytime temperature of 33.2°C (SMHI n.d.a).

To better understand the UHI and IUHI effect and its impact on human health, researchers have increasingly turned to remote sensing, Geographic Information Systems (GIS), and temperature modeling. In this context, remote sensing, GIS, and temperature modeling have become essential tools for monitoring and analyzing land cover changes and their effects on air temperature and human health (Vulova et al., 2020; Lillesand et al.,2015). Remote sensing offers a unique opportunity to monitor urban areas at different spatial and temporal scales, enabling researchers to examine the relationship between land cover changes, urbanization, and UHI at different scales (Zipper et al., 2016; Vulova et al., 2020). Temperature modeling can help identify hotspot areas of air temperature and guide urban planning efforts to implement effective mitigation strategies to reduce the negative impacts caused by high temperatures (Voluva et al., 2020). One such model is The Air pollution Model (TAPM), a model developed by the Australian CSIRO Atmospheric Research Division and is an three-dimensional, prognostic air pollution and meteorological model that uses the equations governing the dispersion of pollution and atmospheric behavior. For metrological studies TAPM uses large-scale weather information (weather forecast or synoptic analysis) and predicts metrology and air pollution at local-, city-, or interregional scales (Hurley ,.P.J. et al 1999 and 2005: Chen, M.D. et al. 2002).

2. Aim and research questions

The objective of this thesis is to examine the correlation between alterations in land cover and nocturnal air temperatures in Helsingborg. Additionally, it seeks to determine whether the occurrence of high temperatures (>18°C) has been influenced by changes in land cover. GIS and remote sensing techniques along with the temperature model TAPM, will be employed to analyze spatio-temporal patterns of land cover and air temperature in the urban area of Helsingborg, Sweden. The meteorology that is to be used in the modeling will be based on the temperatures during summer 2018 due to the high measured temperatures that occurred then. The research questions are as follows:

- How has the Land Cover changed, in Helsingborg, since 2004?
- How does TAPM infer differences in temperature between different land cover types on a local scale?
- How does the alteration in Land Cover affect the nocturnal air temperatures in Helsingborg according to TAPM?

3. Study Area

Helsingborg city (56°2'48.23"N, 12°41'39.73"E) is the central town in Helsingborg municipality, located in the county of Skåne, Sweden (see figure1).Populationwise, Helsingborg is Sweden's eighth largest municipality (SCB, 2022), with a population of 150 109 inhabitants in 2021/2022, and by 2035 it is expected to have reached approximately 170,000 (Helsingborg, 2022).

Figure 1 *shows the location of the urban area of Helsingborg*

Helsingborg is located by Öresund, the strait between Skåne and Själland which is a part of the national border between Sweden and Denmark. The city is influenced by *coastal climate,* which according to SMHI (2011) is characterized by less variations in temperatures, less precipitation and strong winds. Helsingborg has an average temperature of approximately 18 °C during the summer and 0.5 °C during winter. (ibid).

The main focus of this study is Helsingborgs' Urban Area (Swedish translation. *Tätort*). To avoid confusion, further on the city of Helsingborg will be referred to as simply "Helsingborg". As illustrated in Figure 2, the surface area of Helsingborg has changed between 2004 and 2020. The urban area has gone from 38.4 km2 in 2004 to 41.2 km2 in 2020. The study will analyze changes in relation to the city's agglomeration size for each year under study, resulting in slight variations in sizes of study area.

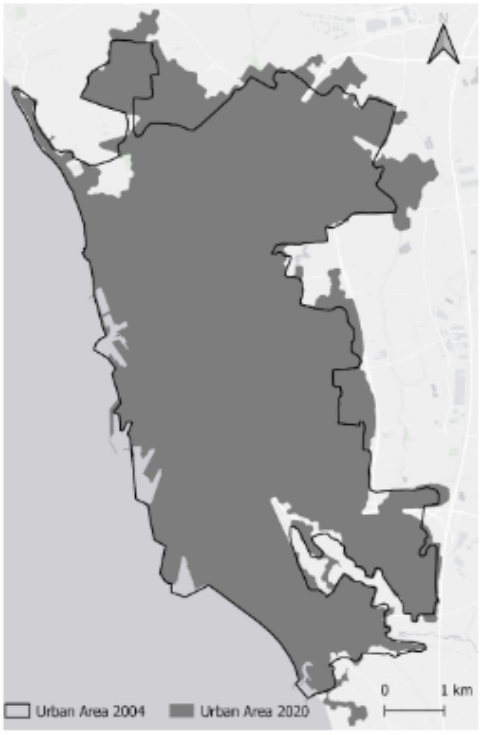

Figure 2 *displays the change in the surface area of the urban area between 2004 and 2020.*

4. Background

4.1 Air temperature

Air temperature (T_a) is a parameter used to characterize weather conditions, and its intensity varies according to seasonal changes (Onomura et al. 2016). T_a measures the kinetic energy of the molecules that make up air, with higher temperatures corresponding to faster molecular motion (Fondriest, 2010). Air temperatures and IUHI are influenced by several meteorological variables, whereas wind speed and cloud coverage has been found to be two of the most significant variables (Onomura et al. 2016). According to a study made by Yokobori and Ohta. (2009) moderate wind conditions (< 3 m/s) are associated with higher nocturnal air temperatures, while an increase in wind speed to > 3 m/s is often accompanied by a decrease in air temperature. Similarly, air temperature tends to be higher when cloud cover is less than 60%, and decreases rapidly when cloud coverage exceeds 60% (Ibid). According to Savage, M.J. (2016) air temperature often reaches its minimum (T_{min}) around sunrise, under clear, calm and mist free conditions.

4.1.1 Land Surface Temperature and Screen-Level Temperature

Air temperature can be measured and documented through various methods. One common approach involves measuring the surface temperature, commonly known as the land surface temperature (LST). LST is measured directly on the surface of the ground and differs depending on the land cover. One of the most used ones for describing air temperature is screen-level temperature or sometimes referred to as near-surface temperature (T_{m2}) since it is measured at 2 meters above ground level, which makes it relevant when studying human temperature exposure (Oke,. et al. 2017: Good. 2016). T_{m2} is an important variable in climate and weather science and finds numerous applications in various fields, including climate change research, and in the evaluation of numerical climate models and weather predictions (Oke,. et al. 2017: Good. 2016).

Under certain conditions the difference between LST and T_{m2} can be as close as < 1 °C, but often there are significant differences between the two variables, with variations of several degrees or more. Whereby the largest difference occurs on clear daytime conditions during the peak of the diurnal temperature cycle. However, LST is lower during night since it often has a direct response to change in solar radiation (Oke,. et al. 2017: Good. 2016). Since LST

tends to be lower than T_{m2} at night it has been determined that only T_{m2} will be considered for this thesis. Further on T_{m2} will be referred to as simply T and in terms when "air temperature/temperature" is mentioned it is T that it referred to.

4.2 Nocturnal Air temperature and Human Health

As previously mentioned UHI and IUHI has a negative impact on human health. High temperatures in cities can lead to heat stress whereby infants, elderly and people with cardiovascular diseases are groups that are particularly vulnerable (Vulova, S. et al 2020: Huang. K. 2019: Majeed H and Floras JS. 2020). Heat stress is a physiological response of the human body trying to maintain normal body temperature, e.g by sweating. This in result may lead to dehydration and in severe cases, heat stroke. However, nighttime generally means lower air temperatures and thus facilitates recovery from high daytime temperatures by reducing physiological stress. High nocturnal temperature can therefore have a severe negative impact on human health if it hinders the possibilities for cooling down (Thorsson et al. 2014: Vulova,et al. 2020). Two relatively new studies by Błażejczyk, K. et al (2019) and Tomczyk AM. (2018) states that nights with a minimum temperature (T_{min}) > 18°C are to be classified as hot/warm nights and nights with a T_{min} exceeding >20°C, it is considered a tropical night. The studíes made stated that temperatures reaching > 18°C were harmful for human health and increased the risk for heat stress. According to IPCC's (2022) report, Sweden will be significantly impacted by climate change through increased temperatures. By 2030, heat waves in Sweden are projected to be 4.1 times more frequent than before, corresponding to the temperatures measured in summer 2018 raising the risk of heat stress for urban dwellers throughout the country (ibid).

4.3 Urban Land Cover and its effect on air temperature

Urban climate is affected by the spatial variation of the urban geometry i.e *fabric*, *surface cover* and *structure*. The structure of the urban area influences the *albedo*, regulating radiative patterns and the exchange of airflows through the city. The urban geometry determines the urban surface's ability to reflect, absorb and emit radiation but also its ability to retain and/or transfer heat and water into the atmosphere and the effects that it has on the urban climate. The cooling rates of urban land cover (surface) vary based on their radiative

properties, and they exert diverse influences on the nocturnal intensity of the UHI (Oke.et al. 2017).

Built-up areas, such as paved surfaces and buildings, are significant contributors to the Urban Heat Island (UHI) and the Intra-Urban Heat Island (IUHI) effect. During the day, these surfaces absorb solar radiation, storing heat energy (radiation). At night, they release this stored radiation, leading to increased temperatures in urban areas (Lan, Y and Zhan, Q. 2017). Studies have shown that, dry and open spaces covered in grass tend to cool rapidly during night, in relation to hard built-up surfaces (Spronken-Smith and Oke. 1998; Yokibori & Ohta.2009; Onomura.2016; Oke et al., 2017; Konarska et al. 2016; Hart & Sailor. 2009). According to Spronken-Smith and Oke. (1998) dry vegetated urban parks tend to exhibit 1-3 °C lower temperatures during night then surrounding built up areas and is causing a so-called "Park Cool Islands" (PCI). On the other hand they also found that open grass surfaces can sometimes exhibit higher nocturnal air temperatures than the surrounding urban areas and nearby dry parks, due to the soil moisture. Wet soils/irrigated grasslands, in particular, tended to be warmer at night because of the higher thermal admittance of water during the night-time period (ibid). In their study on temperature behaviors during hot summer conditions in Tel Aviv (Israel) Potcher, Cohen, and Bitan (2006) examined urban parks and observed that grass-covered parks lacking significant tree coverage tended to experience higher temperatures during daytime, and sunlit conditions, compared to their surrounding areas and parks with a more substantial tree canopy cover. However, during nighttime, the presence of medium-sized, densely planted trees in parks contributed to uncomfortable climate conditions and increased heat due to elevated humidity levels and enhanced wind velocity

Trees have been shown to be one of the most effective natural ways to cool urban environments during the day. They generate shade, prevent solar radiation from reaching the ground and by evapotranspiration they release water vapor into the air, increasing the relative humidity which contributes to decreasing air temperatures (Konarska et al. 2016; Thorsson et al., 2014). Wujeska-Klause and Pfautsch (2020) conducted a study on the effect of trees with broad dense canopy covers (31%) and low canopy covers (11%) on air temperature during the day and night. The study found that trees with dense canopies were effective at reducing temperatures during the day compared to trees with low canopies. However, during the night, the trees with dense canopy covers had an opposite effect, where heat was trapped underneath

the canopy and increased the air temperature, due to limited transpiration during night and low ventilation underneath the canopy. Whereby trees with low canopy covers tended to have a higher ventilation and allowed the movement of *longwave radiation* (outgoing radiation that has been stored in objects/surfaces during day), decreasing the air temperature during night, this is illustrated in figure 3.

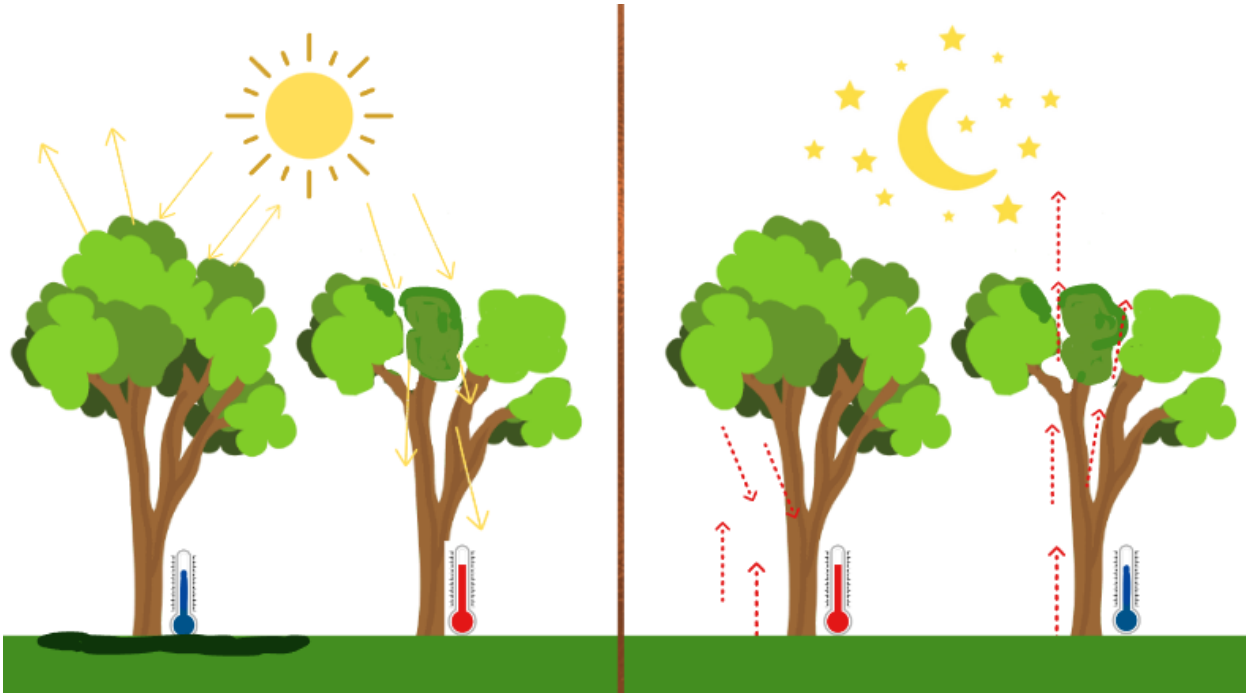

Figure 3. *Illustration of the difference between dense canopies and low dense canopies during day (left) and night (right). Source: Wujeska-Klause and Pfautsch (2020). Image modified by: Amanda Bäck (2023).*

4.4 The Air Pollution Model - TAPM

As previously mentioned, TAPM is a comprehensive prognostic model for air pollution and meteorology, operating in a three-dimensional framework. It employs equations that govern the behavior of pollution and the atmosphere. For meteorological inputs TAPM uses large-scale weather information and predicts metrology at different scales. The model encompasses a range of parameters associated with physical processes, including rainfall, wind patterns, sea-surface temperature, soil temperatures, solar radiation fluxes, and air temperature. Notably, TAPM is a dynamic model, meaning it continuously adjusts its processes and adapts to changing input data over time (Hurley et al. 2008; Chen M.D et al. 2002).

An important consideration prior to employing TAPM is assessing if the model is applicable to the Swedish climate. Chen M.D. et al. (2002) conducted a study to investigate the applicability of TAPM on the Swedish west coast, followed by a validation process. The validation demonstrated that TAPM adequately modeled air temperature and horizontal wind at a height of 2 meters, showing a strong correlation ($R2 = 0.92$) and low squared error ($<0.05°C$) for modeled and observed temperatures. However, the model consistently underestimated surface temperature by approximately 1°C. Regarding surface wind, although the correlation coefficients were slightly lower ($R2 > 0.60$) compared to temperature, the model performed well. The study concluded that TAPM is suitable for the Swedish climate and proficient in modeling urban heat islands and sea/land breeze.TAPM can utilize up to five nested grids for calculations (Hurley, 2008), with the study by Chen M.D. et al. (2002) employing a tree range nesting grid at 9 km, 3 km, and 1 km resolutions. Therefore, it is of great interest to determine if TAPM can achieve a similarly high coefficient of determination with a finer spatial resolution at 100x100m.

5.Methodology

The methodology and materials used in this study are based on COWI's "GIS Analysis and Climate Adaptation Project," conducted at the request of the County Administrative Board of Skåne. The project's objective was to investigate the influence of land cover and land use changes on climate change effects in urban areas. It encompassed seven urban areas in Skåne, including Helsingborg. With the exception of observed meteorology, all data utilized in this study were provided by COWI.

While the project employed a range of methods, this study specifically focuses on generating additional information pertaining to the selection of vegetation and land use types, as well as grid settings for TAPM. Therefore, there will be variations in TAPM settings between this study and COWI's project. In contrast to COWI's utilization of a 400x400 grid and distinct vegetation and land use classes for grassland, this study employs different approaches and classifications. The following section will present this study's methodology and will be divided into two parts - Land Cover Classification (*part 1*) and Temperature modeling (*part 2*).

5.1. Land Cover Classification

5.1.2 Data for land cover classification

Data presented in table 1 were provided by COWI and origins from Lantmäteriet and SCB.

Table 1. *Showing data used for the Land Cover Classification..*

File Type	Spatial resolution	Spectral Bands	Year	Source
Orthophoto 1	1 m	3 (RGB)	2004	COWI
Orthophoto 2	1 m	4 (RGB+IR)	2020	COWI
Shapefile for urban area (tätort)	-	-	2004 & 2020	COWI

Unfortunately, the metadata of the orthophotos did not include information about the specific time period when they were taken. To overcome this limitation, the analysis focused on assessing the canopy cover of trees and grassland visible in the photos. Upon examination, it was observed that the majority of trees exhibited dense canopy covers and appeared to be deciduous. Based on these visual observations, it was inferred that the photos were likely captured during a similar time period. Consequently, they were deemed suitable for

comparison and image classification purposes. The orthophotos provided underwent resampling to achieve a uniform resolution of 1 meter across all years. This resampling process was employed to mitigate potential errors arising from variations in land cover analysis throughout the studied period

5.1.3 Image classification

Image Classification (IC) plays a crucial part in the field of Remote Sensing, image analysis and pattern recognition i.e. when studying land cover or land use mapping. Image classification is the process of assigning *informational classes/categories* to *multipixel objects*. It is the process of matching spectral categories to informational categories in an image. Informational classes are categories of interest to the analyst i.e different kinds of land use/land cover or different types of geological units (Campbell, J. B., Wynne, R. H., & Thomas, V. A., 2022). One way that has become increasingly common to use when conducting image classification and has shown obtaining high accuracy, is pre-trained deep learning models that use *Artificial neural network (ANN) algorithms*. ANN classifiers use pattern recognition systems and have shown to be versatile when it comes to combining different types of datasets, making them suitable to integrate in GIS and remote sensing (S. Mohan, Giridhar, M.V.S.S. 2022).

One such pre-trained model is the *High Resolution Land Cover Classification* (HRLCC) model. The model utilizes orthophotos as inputs, with specific criteria including an 8-bit format, a resolution of 80-120cm, and a minimum of 3 spectral bands. Although the model was released in 2021 (Esri, n.d.), there is limited scientific literature available regarding its publication or detailed information.

Using the HRLCC model is a straightforward process. Once the model's license has been downloaded and all the orthophotos have been added to ArcMap Pro, the procedure can begin. To be able to run the model, the orthophotos for each year are used as an input and cell size is set as 1 x 1 m. The processor type defaults to its optimal setting, and running the model is as simple as clicking the "Run" button. The resulting Land Cover image will appear shortly after.

5.1.3.1 Accuracy assessment

An accuracy assessment was conducted after the image classification process by creating a confusion matrix. The confusion matrix compares the classified results with the ground truth data, offering insights into correct classifications (overall accuracy, OA), inclusion and exclusion errors (producer's accuracy, PA, and user's accuracy, UA), and the reliability of the classification (kappa coefficient, K) (Congalton & Green, 2009; Lillesand et al., 2015). For more details on image classification and confusion matrices, see Appendix 1.

A total of 500 randomly selected assessment points were used to minimize bias and achieve a high accuracy assessment. The number of units per category was not predetermined due to the random sampling strategy. However, to ensure reliable results, the categories "trees," "grassland," "paved surface," and "buildings" had more than 50 sample units each, following the recommendation of Congalton & Green, 2009. "Water" and "bare soil" categories, covering small areas, were given less priority in the confusion matrices. For each assessment point, both a classified value and a ground truth value were assigned in the attribute table. The classified value represented the ID from the classified images, while the ground truth value was determined manually by examining orthophotos. After assigning ground truth values to all points, the confusion matrix was generated. To ensure further analysis in TAPM, the classification needed to achieve an overall accuracy (OA) over 85%.

5.4 TAPM

The following section will explain the method for the temperature modeling. Figure 4 shows a brief overview of the method and will be further explained in the text.

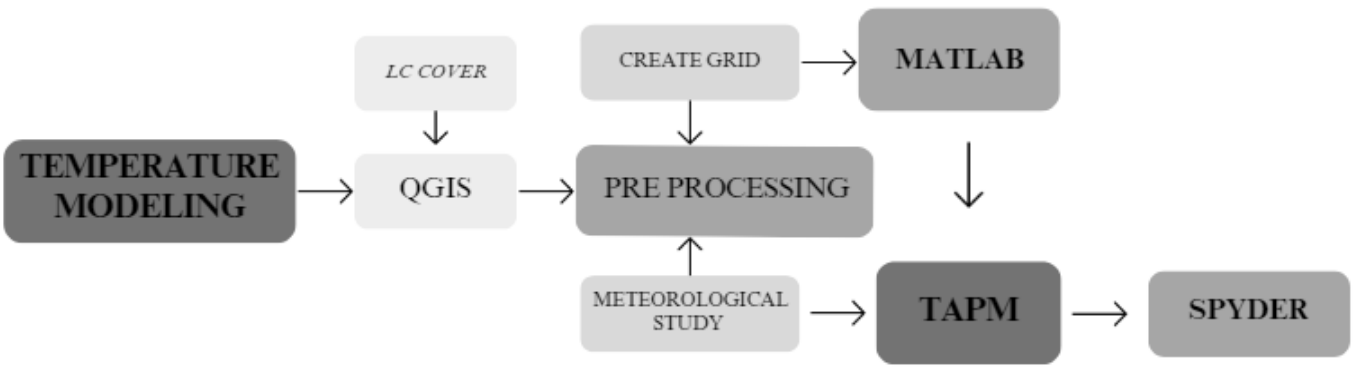

Figure 4. *An overview of the steps for this project leading up to the use of TAPM.*

5.4.1 Data for temperature modeling

In order to compute the temperature modeling in TAPM data presented in table 2, is required.

Table 2. *Data used for the temperature modeling.*

Data	File type	Year	Source
.veg files	Land Cover	All years	created by the Author
.ter file	DEM	2010	COWI
.ERA5 files	Meteorology	2018	COWI
Observed Meteorology*	Meteorology	2018	SMHI a and b

** will be used to compare the modeled temperature and wind speed in TAPM.*

The terrain file (.ter) was provided by COWI and is the same DEM that was used in the COWIs project. It is 50x50 m and is based on the terrain from 2010, due to the unavailability of suitable terrain data, it was decided to use the 2010 DEM for all years. Since TAPM will change the terrain file, this was not considered a problem.

Even though TAPM does not require site specific land cover or meteorology, additional information was added to improve the modeling precision. Since this study aims to study the temperature on a local scale, in this case 100 x 100 m, the land cover must be the same size. To do that, a new .veg file (Land Cover) must be created. The vegetation file (.veg) are based on the result from the land cover classifications but were generated by creating a grid with a 50 x 25 resolution and computing *zonal statistics* with the *majority function* in Qgis. This was then saved as a textfile and transferred into Matlab to create a numeric matrix which included one value for each 50x25m square, making up the actual land cover, but now with a 50x25 m resolution, and saved as a .veg file. The .veg file is then used as input in TAPM, where it is remade and runned with majority filter once again (within TAPM) with a grid at 100 x 100 m. An example of how the transformation of the LC from 1x1 m to 100x100m are shown in figure 5, where A represents 1x1m, B represents 50x25 m and C represents 100 x 100 m.

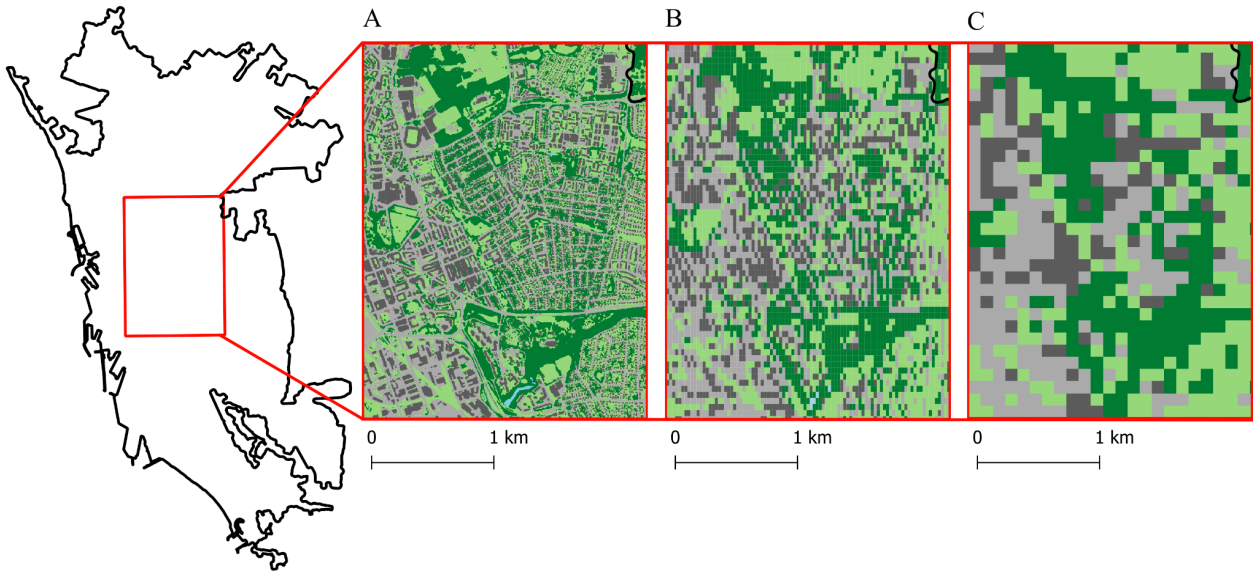

Figure 5. *Example of the development of the land cover layer from the image classification (1m) to TAPM (100m).*

Additional meteorology data in the form of ERA5 files, were used. ERA5 are global atmospheric reanalysis datasets which are a result from combining meteorological observations and model data. The files are developed by the *European Centre for Medium-range Weather Forecasts* (ECMWF), and consist of hourly estimations for numerous atmospheric, oceanic-wave, and land-surface variables (Hersbach, H. et al. 2018). These files are used as meteorological input data in TAPM.

5.4.2 Meteorological study - observed data

During summer 2018, July stood out as exceptionally hot, and Helsingborg recorded its highest temperature since 1951 on July 26th, reaching a daytime temperature of 33.2°C (SMHI n.d.a). It was decided to include that night and the surrounding days in the study period, whereby three warm nights and one colder night were identified and used. ERA5 were used as input in TAPM to examine the impact of land cover changes between 2004 and 2020 on nocturnal temperatures. Observed meteorological data from SMHI, n.d a and b (see Appendix 2 for the meteorological station locations), were collected to determine the study period and to compare the correlation between observed data and TAPM modeling. The coordinates of the observed meteorological station were used as input into TAPM to extract an XML document, enabling the comparison of datasets at the same location.

Since cloud coverage and wind speed are crucial variables influencing T, observed data were used as a reference to identify nights for study, aiming for calm and clear conditions (cloud cover < 60% and Wind speed < 4m/s). Unfortunately, specific information on observed cloud coverage was not available, and it was also absent from the ERA5 dataset. To address this limitation, precipitation data was used as a proxy for cloud coverage.

The study period selected for analysis included nights from July 25 to July 30, 2018. Among these nights, only July 28th and 29th had observed precipitation data, while the remaining days and nights were precipitation-free (0 mm/h). Since it was confirmed that the particular night of July 28th did not have clear conditions, it was excluded from the visualization. Therefore, the nights visualized in the study are July 25-26th, 26-27th, 27-28th, and 29-30th. It is worth noting that the night of July 29-30th exhibited lower temperatures (T °C) compared to the other nights, as shown in figure 6. Although this lower temperature may suggest non-clear conditions, it was not confirmed, and thus the night was still included in the study. The night of July 29-30th (the coldest night) is considered representative of a "normal" summer night and was therefore of interest to include in the analysis.

To analyze the nocturnal temperatures, three specific UTC hours: 19:00, 22:00, and 03:00 were chosen. The selection of these hours was based on the sunset and sunrise times for each night. In Swedish local time, sunset occurred between 21:19 and 21:21, while sunrise was around 04:59 (03:00 UTC). Since the temperature data provided hourly outputs, the hours coinciding with sunset and sunrise were chosen for analysis. 19:00 UTC is therefore 20 min before the sun has set. Figure 6 illustrates the observed temperature during the study period. The "boxes" in the chart represent the study period, right before sunset at 19:00 UTC and sunrise at 03:00 UTC. The box for July 28-29 is marked in red to indicate its exclusion from visualization. However, it's important to note that this day/night will still be included in TAPM’s calculations

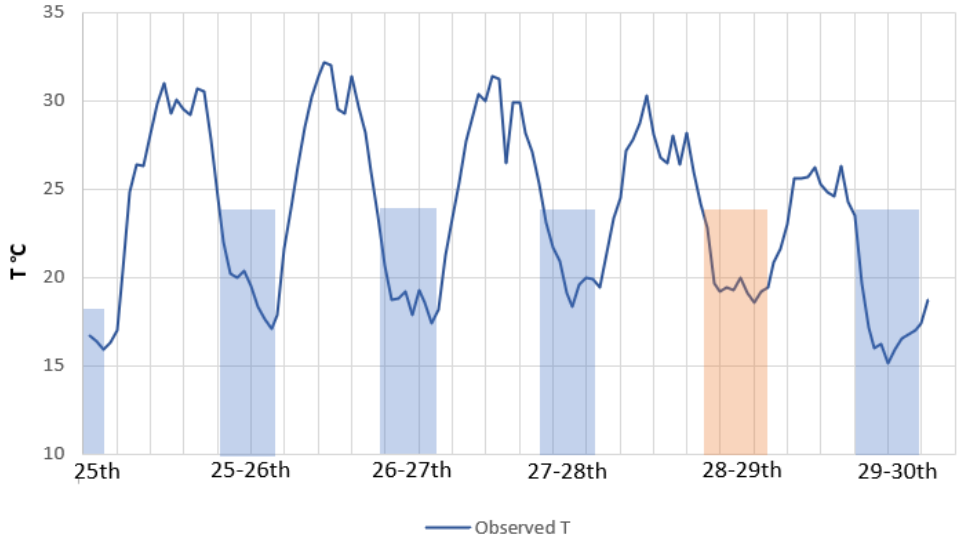

Figure 6. *Air temperature through 25 to 30th of July 2018. The boxes symbolize the study period 19:00 UTC to 03:00 UTC. The night between 28-29th is highlighted with a red box, indicating that that night is excluded from the visualization of the data.*

5.4.3 Settings and LC-types in TAPM

TAPM uses default values and variables for vegetation types and land use classes which are based on a CSIRO Wildlife and Ecology Categorisation (Hurley. P,. 2008). Table 3 shows some of the vegetation and land use types and their variables such as: vegetation height (h_f) , fraction of surface covered by vegetation (σ_f), Leaf area index (LAI), minimum stomatal resistance s^{-1} (r_{si}), Urban Albed (α_U), Vegetation Albedo (α_f) and Anthropogenic heat flux (A_u) that are being used in TAPM and for this study. If there is an interest in examining the full list of vegetation types and land use, please refer to appendix 3 or read Hurley, P,. 2008. Further on the LC-types will refer to the name that it says under the headline "Category" in table 3.

Table 3. *Some of the vegetation- and land use classes in TAPM. Source: Hurley. P,. 2008*

ID	Veg-Type (TAPM)	h_f (m)	σ_f	LAI	r_{si}	α_U / α_f	A_u	Category
0	Water	-	-	-	-	-	-	Water
4	Forest mid-dense	17	0.50	3.8	200	0.20	-	Trees
18	Grassland -dens tussock	0.75	0.75	2.3	150	0.20	-	Grassland
27	Pasture/herb field - sparse*	0.30	0.25	1.0	80	0.20	-	Bare soil
32	Urban Low**	8	0.75	2.0	100	0.17	20	Paved surf.
34	Urban High	16	0.75	2.0	100	0.13	40	Buildings

** This was used as TAPM does not have any LC type for bare soil*
***This was used as TAPM does not have any LC type for paved surfaces*

Fraction of surface covered by vegetation (σ_f) %: According to Copernicus (2022) the Fraction of Vegetation Cover (F_{Cover}), is a metric that indicates the percentage of the ground that is covered by green vegetation. Essentially, it measures the spatial distribution of the vegetation.

Leaf Area Index (LAI): is a measure of vegetation and refers to the total ratio of leaf area to the corresponding surface area, and can measure four times larger than the ground surface. LAI is commonly used to describe the density of vegetation canopies (de Blij et al. 2013).

Minimum stomatal resistance (r_{si}) m^{-1}:Minimum stomatal resistance refers to the minimum amount of resistance that a plant's stomata (small pores on leaves, controlling evaporation) can offer to the movement of water vapor out of the leaf and helps plants to conserve water. It is a measure of how open or closed the stomata are, and is influenced by various environmental factors such as light, temperature, humidity, and soil moisture. A lower minimum stomatal resistance indicates that the stomata are more open, allowing for greater water loss through transpiration. Whereby a high stomatal resistance indicates low release of water vapor (Monteith J. L. et al. 1965).

Urban Anthropogenic Heat Flux (Au) W/m^2: The Au is the heat generated by the consumption of biological, chemical, and electrical energy by human activities in an urban area that is being released into the atmosphere (Liu Yiqing et al. 2022)

Urban (α_U) and Vegetation (α_f) Albedo: The reflectivity of an object/surface, the higher the albedo the higher the reflectance and less heat storage (de Blij et al. 2013).

To achieve the highest possible resolution, a four-nested approach was implemented to create grid domains of 6.4 km, 1.6 km, 0.4 km, and 0.1 km. This approach ensured consistency in vegetation files and other input data sizes within the specific grid of interest, which in this study is grid 5 (100x100m). The sea surface temperature setting was based on observed data from Helsingborg's measuring station for SST, with a value of 293.2 Kelvin (20.05°C) (SMHI, n d b). Default values for deep soil temperature and deep soil moisture for the month of July were used, set at 289.6 K (16.45 °C) and 0.15 respectively. A three-day spin-up period was chosen to allow the model sufficient time to adjust all settings before generating the output data. Once the model had been runned and generated output data, the output files were processed using Spyder to convert the output files to grid files so they could be viewed and analyzed in Qgis.

5.4.4 Change detection maps

One method for analyzing changes that occur over time involves performing change detection, which can be referred to as post-classification comparison when applied to classified images (Lillesand et al. 2015). The comparison is done by layering the classified image and letting the computer detect pixels whose classification category has been changed from one to another, between the different datasets. In addition, change maps and statistics can be compiled to express the nature of the specific changes. e.g by highlighting areas that have changed from category A to category B (Ibid). This was done by using a raster calculator - subtracting the 100x100, 2020 LC layer with the 100x100, 2004 LC layer.

6. Results

In order to calculate the impact of changing urban land cover and buildings on nighttime air temperature, the approach employed in this study includes the utilization of the HRLCC model for image classification to obtain relevant input for meteorological modeling. As a result, this chapter is structured into three sections to comprehensively address the research objectives. Firstly, the results regarding the land cover classification methods and the changes in land cover in Helsingborg will be presented, including the accuracy assessment. Secondly, the change detection maps will be presented to see how vegetated and non-vegetated surfaces have changed between the years. In the final section, the result from the temperature modeling will be presented which will end in an analysis of nocturnal air temperature and the correlation to land cover and air temperatures at a 2m height.

6.1 Image Classification

The deep learning method generated two LC layers which are presented in figure 7. According to the accuracy assessment the image classifications reached higher than the desired overall accuracy for >85%, whereas the classification of the 2004 orthophoto reached 90.4 % and the classification for the 2020 orthophoto reached 93.6%, indicating a strong agreement with reality. The results from the accuracy assessment are presented in table 4 and 5.

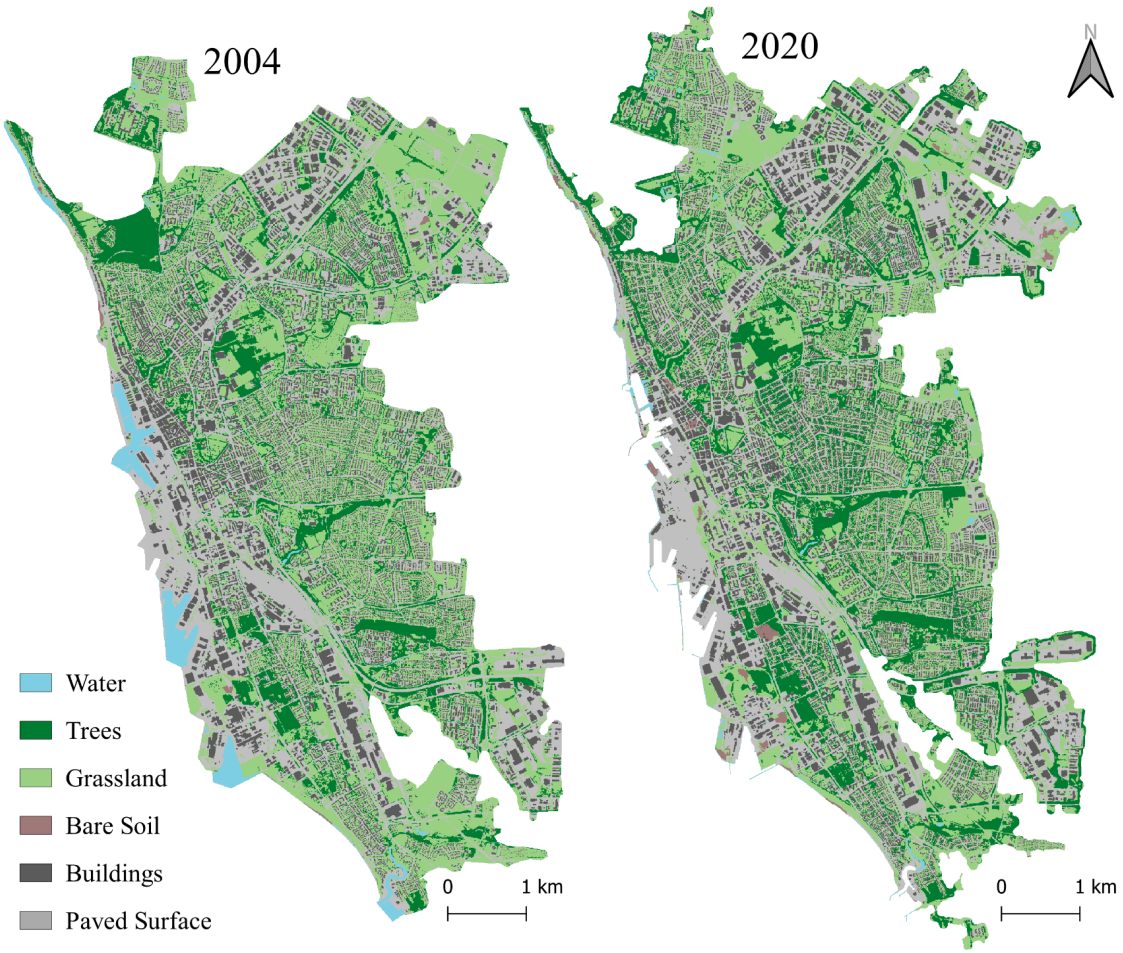

Figure 7. *Results from the Deep Learning Image classification.*

Although the Overall accuracy (OA%) is high, there is also a notable Kappa value, implying that the classifications were performed accurately rather than by chance (see appendix 1 for explanation about Kappa). Upon examining the confusion matrices presented in tables 4 (2004) and 5 (2020), it can be inferred that there are significantly few omission and commission errors, indicating that the classification has succeeded well (see appendix 1 for explanation about commission and omission errors).

Table 4. *Confusion matrix for the image classification made for 2004. Class value 4 = trees, 18 = grassland, 27 = bare soil, 32 = paved surface, 34 = buildings and 0 = water.*

Class Value	**0**	**4**	**18**	**27**	**32**	**34**	**Total**	**UA**	**Kappa**
0	**7**	0	0	1	0	0	8	87%	0
4	0	**58**	6	1	1	0	66	88%	0
18	0	9	**160**	6	5	4	184	87%	0
27	0	0	0	**0**	0	0	1	100%	0
32	0	0	4	4	**148**	5	161	92 %	0
34	0	0	0	0	2	**79**	81	98%	0
Total	7	67	170	12	156	88	**500**	0	0
PA	100%	87%	94%	0%	95%	90%	0	**90%**	0
Kappa	0	0	0	0	0	0	0	0	**87%**

Table 5. *Confusion matrix for the image classification made for 2020. Class value 4 = trees, 18= grassland, 27 = bare soil, 32 = paved surface, 34 = buildings and 0 = water.*

Class Value	**0**	**4**	**18**	**27**	**32**	**34**	**Total**	**UA**	**Kappa**
0	**3**	0	0	0	0	2	5	60 %	0
4	0	**92**	4	0	0	0	96	96 %	0
18	0	5	**136**	5	4	1	151	90 %	0
27	0	0	0	**1**	1	0	2	50 %	0
32	0	1	1	2	**156**	6	166	94 %	0
34	0	0	0	0	0	**80**	80	100 %	0
Total	3	98	141	8	163	87	**500**	0	0
PA	100%	94%	96%	13%	98%	92%	0	**94%**	0
Kappa	0	0	0	0	0	0	0	0	**91%**

In figure 8 it is shown how the total area (km²) of each LC type was classified during the image classification. According to the image classification the grassland has decreased in area, from 14 km² to about 13.6 km². Tree covered surfaces have increased by 2.1 km² between 2004 and 2020. Paved surfaces and building covered surfaces have also increased between the years. In order to make a relevant comparison of the LCC between the different years, the change of different classes were also compared to the total area of each year respectively. Water has not decreased, it shows different values due to different sizes in the urban area (see figure 2).

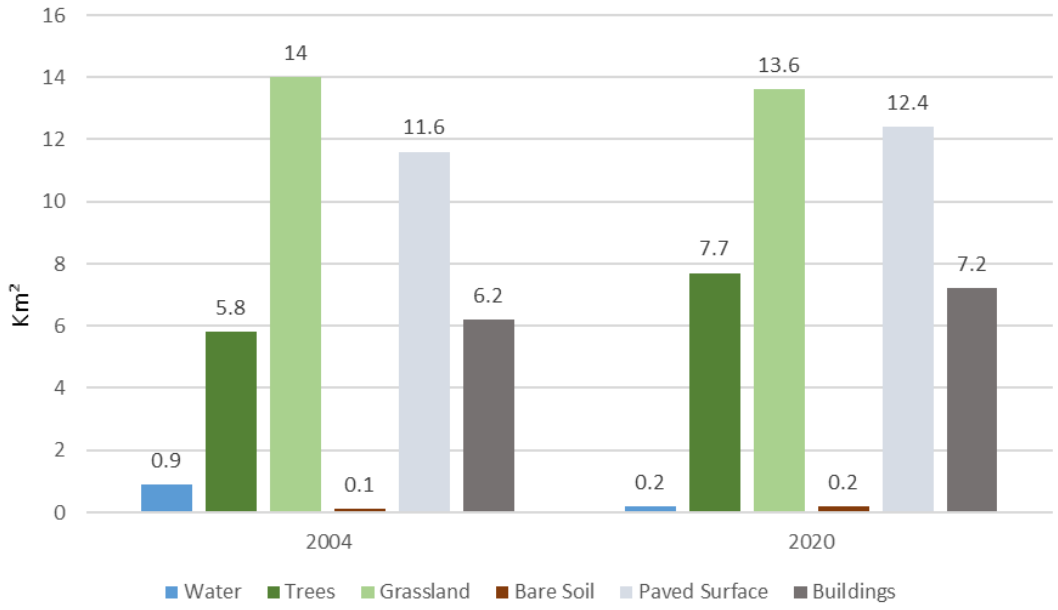

Figure 8. *The classification categories and their total area, during 2004 and 2020, according to the image classification.*

In table 6 it can be seen that in relation to urban area size, percentage wise, the tree covered surfaces have increased by 3.8% since 2004 and grassland has decreased by 3.4 %. This can be due to tree canopies covering grass covered surfaces or indicating that the canopies have grown bigger, that more trees have been planted or that grass covered surfaces have been replaced by other land cover types e.g buildings.

Table 6. *The proportion of each LC-type within the urban boundary for each year i.e 38.4 km2 (2004) and 41.2 km2 (2020).*

	Buildings	**Bare soil**	**Paved**	**Grassland**	**Trees**	**Water**
2004	16.1 %	0.3 %	30.1 %	36.3 %	15%	2.3%
2020	17.4 %	0.5 %	30 %	32.9 %	18.6 %	0.5 %
Change	+ 1.3 %	+ 0.2%	- 0.1 %	- 3.4 %	+ 3.8%	/

6.2 Change detection

Change detection analyses were conducted on both the land cover (LC) layers generated through image classification and the LC layers created in TAPM. These analyses aimed to visualize the changes between the years. Figure 8 presents the 100 x 100m LC, along with the change detection map illustrating the variations in LC between different years as determined by TAPM. The change detection map highlights two areas that have undergone significant LC changes (LCC) - area A and area B, as shown in figure 9. In area A, the predominant change has been from grassland to urban areas, while area B has experienced transitions from grassland to tree-covered surfaces and also from vegetation to urban areas

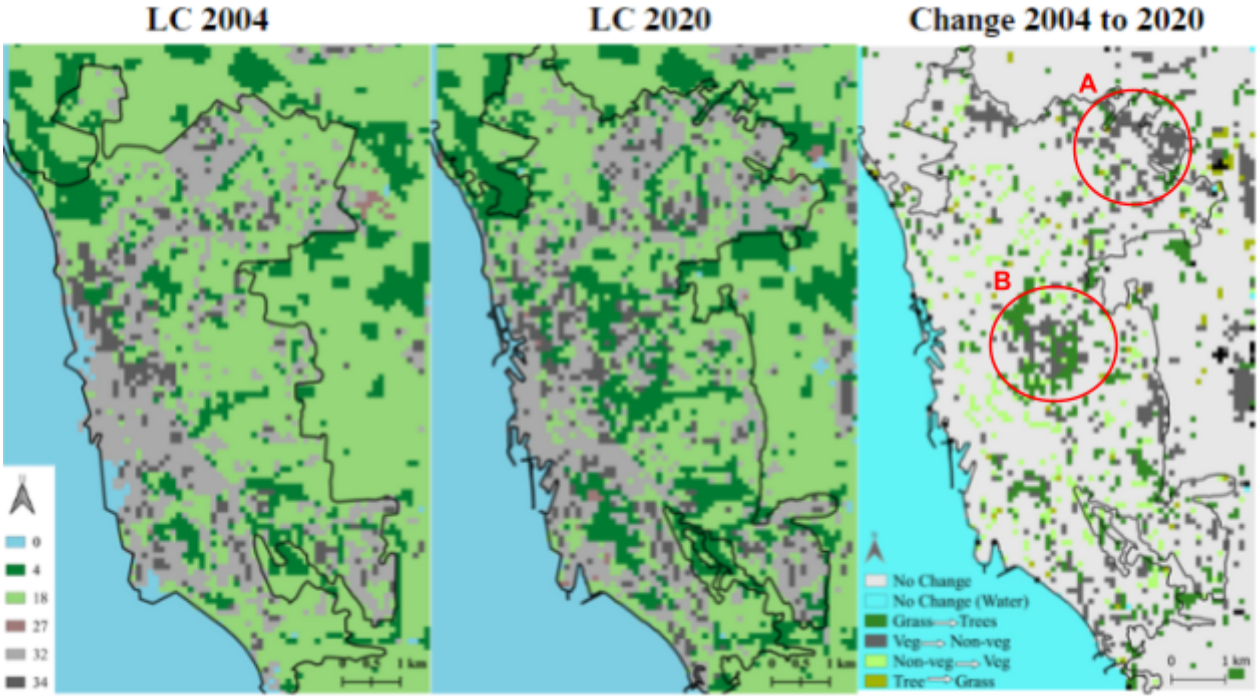

Figure 9. *Land cover, created in TAPM, with 100 x 100m resolution is visualized in the maps named 2004 and 2020. 0 = water, 4 = trees, 18 = grassland, 27 = bare soil, 32 = paved surface and 34 = buildings. The map to the right is a change detection map of the LC between 2004 and 2020.*

6.3 Temperature modeling

6.3.1 Meteorological study and validation of TAPM

The thermal profiles, for observed and modeled T, during the studied nights and the associated days are visualized in figure 9. The boxes indicate the time right before sunset (19:00 UTC) until sunrise before sunrise (03:00). The night between 28-29 is excluded in the visualization and is therefore marked with a red box.

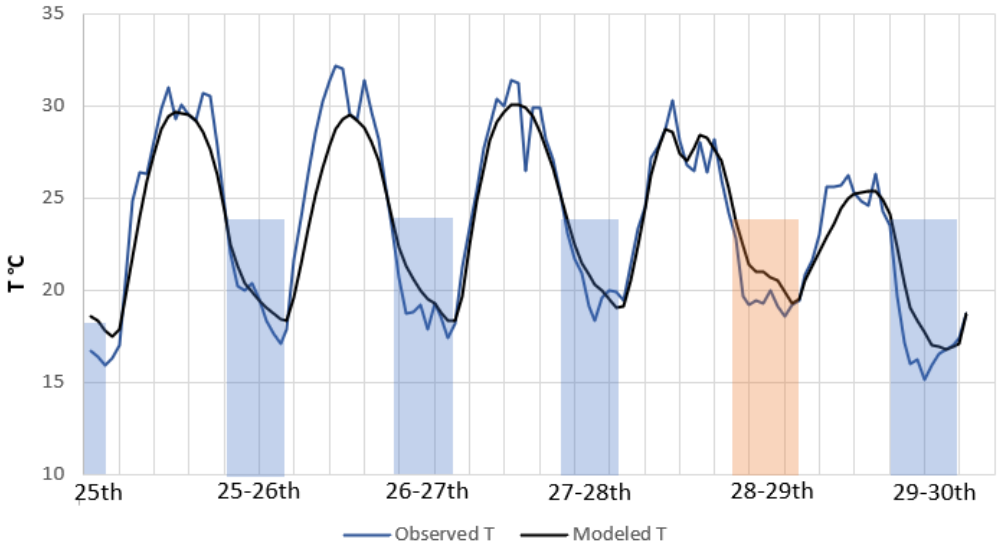

Figure 10. *The thermal profiles for observed and modeled T during the time period 25/7 to 30/7, night and day is shown. The highlighted boxes indicate the study period (nights) Source: SMHI (n.d a).*

In figure 11, the correlation between modeled and observed data (temperature and wind speed) are presented. Whereby, the R2 value for temperature reaches 0.91 and indicates that the modeling accurately captures the temperature variability during the study period. However, when it comes to wind speed and wind direction, the correlation is lower with an R^2 value of 0.58 (see Figure 11).

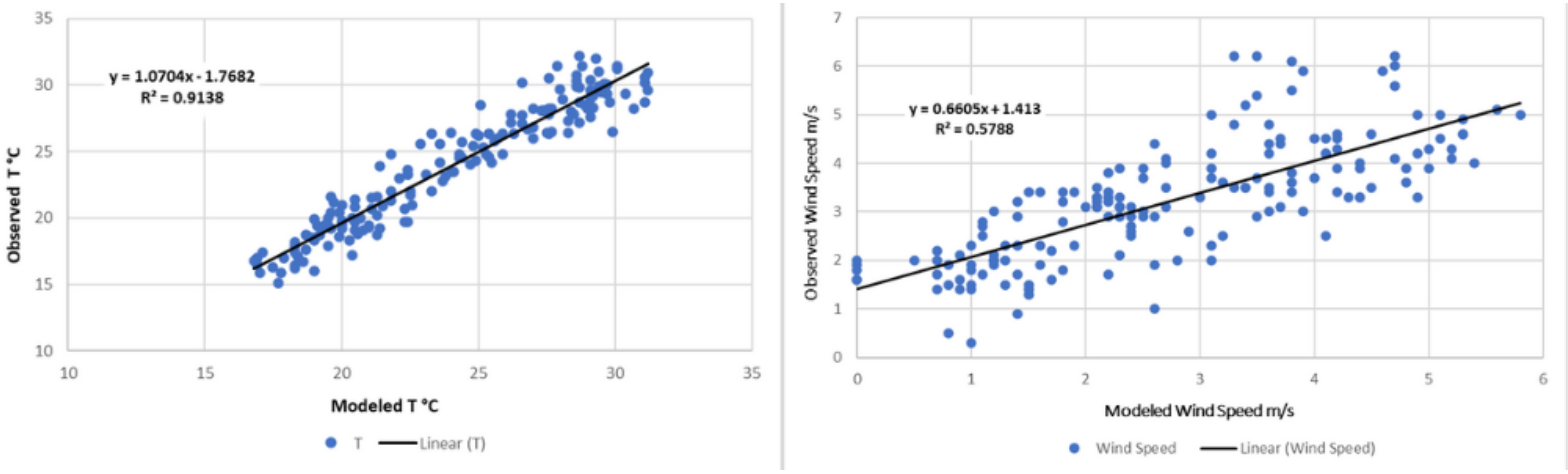

Figure 11. *Scatter plots of the observed and modeled temperature 2 meters above ground level, and wind speed 10 meters above ground level.*

Analysis of the main wind directions between July 25th and 30th, 2018, based on the observed data, reveals that the predominant directions were from the North and South-East. The modeled data, on the other hand, showed a slightly broader range of wind directions, including North, North-West, East, South-East, and South. It is noteworthy that neither the modeled data nor the observed data indicated any wind coming from the South West, meaning no influence from the sea during the study period (see Figure 11).

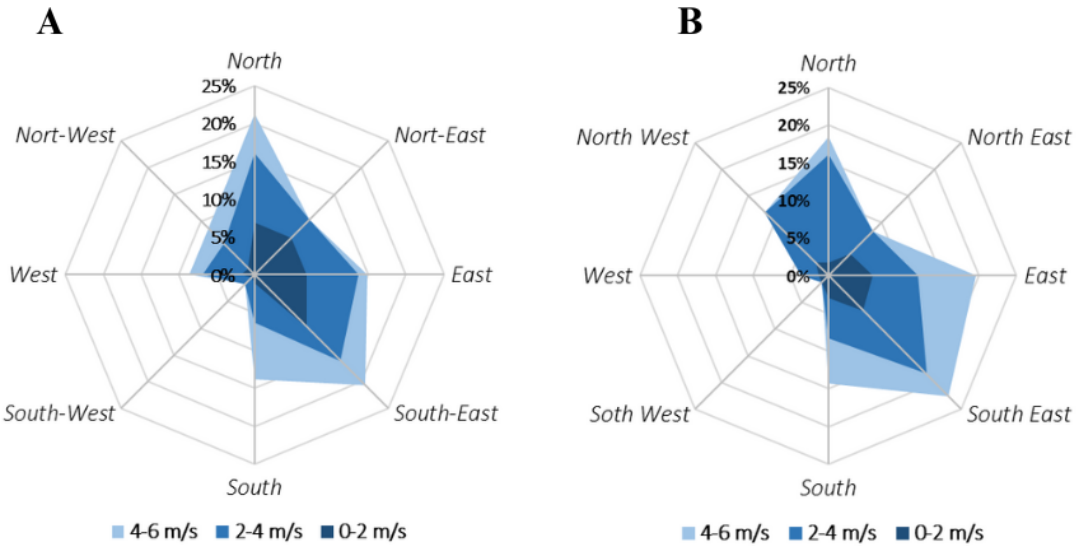

Figure 12. *Two rose chart containing A) observed wind direction and wind speed and B) modeled wind direction and wind speed, 10 m above surface, during night and day for 25/7- 30/7th, is shown. Source: SMHI (n.d a and b).*

As shown in figure 13, containing four graphs with modeled and observed wind speed and temperature, the highest wind speed (3.5 m/s) were observed during the night between 27-28th. Increase in temperature follows the curve of decreased wind speed and vice versa. However, it is also evident that T_{min} for all nights is recorded just before sunrise at 03:00 and gradually increases thereafter.

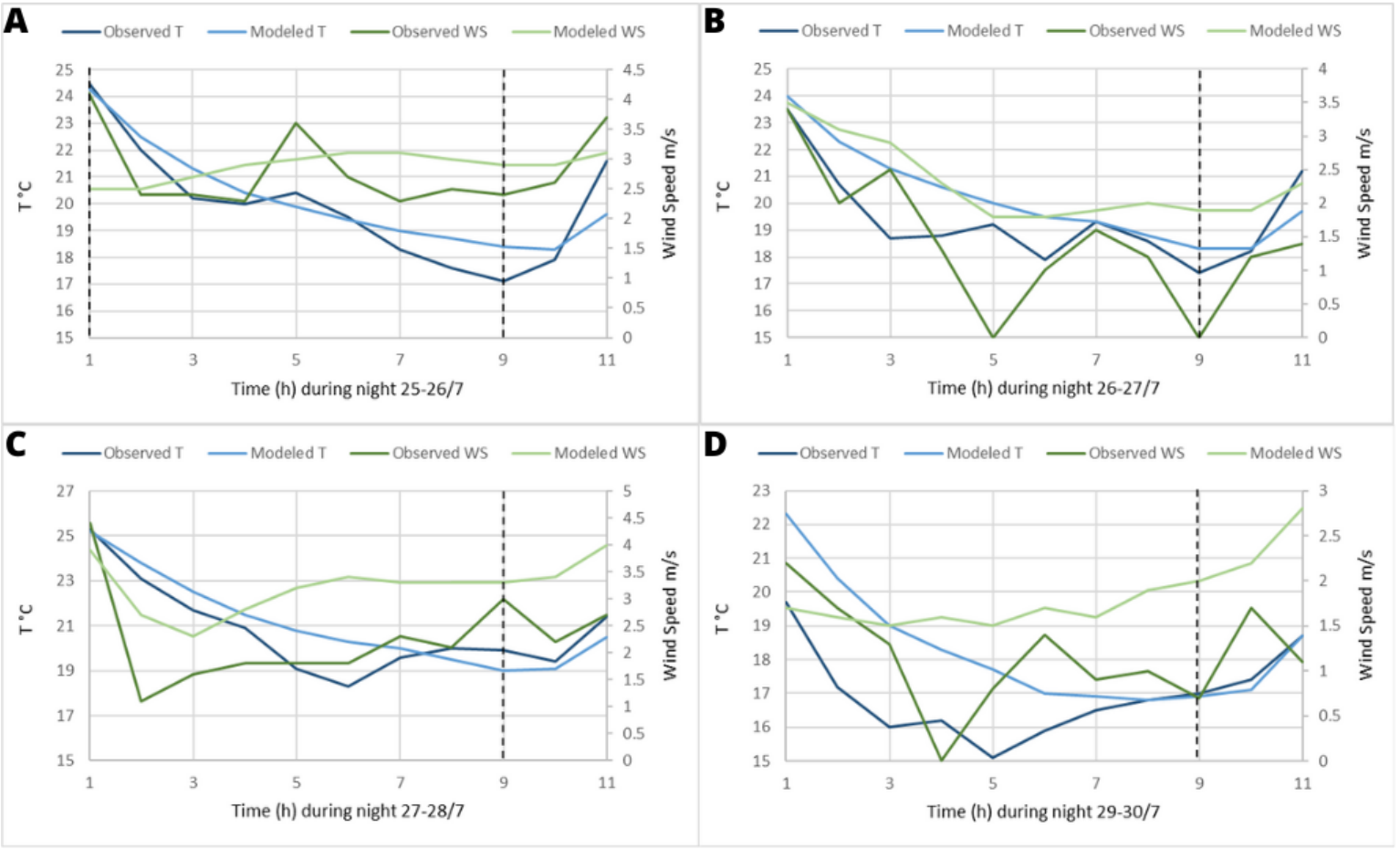

Figure 13. *The observed and modeled T °C, and wind speed for each night. A = 25-26th, B = 26-27th, C = 27-28th and D = 29-30th. The X axis presents the hours of study, whereby h 1 = 19:00 UTC (sunset) and h 9 = 03:00 UTC (sunrise). 22:00 UTC occurs during h 4. Source: SMHI (n.d c).*

6.3.2 Detailed modeling

Based on the land cover analysis and meteorology for the chosen summer days in 2018, the nighttime air temperature is modeled in TAPM. The ranges of the colorbars legends in figures 14,16,18 and 20, were chosen based on T_{min} and T_{max} for each time period and night. Therefore, the maps are not directly comparable between different hours the same nights, thus the same hours for the different nights are having the same temperature spann and are therefore directly comparable. This method was chosen to facilitate the assessment and visualization of how the air temperature changes with land cover between 2004 and 2020 affect the temperature. The figures are therefore easier to compare vertically rather than horizontally.

All nights

In figures 14-21 the results generated from TAPM are visualized. From 19-03 UTC, the variations in the IUHI, between the years and nights are approximately the same and generate similar temperature patterns, hence, table 7 presents the general results for all nights.

Table 7. *Overview of the result during all nights.*

Time at night in UTC	**Temperature Pattern for both years**
19:00	$\mathbf{T_{max}}$ is located over grassland and built up areas → IUHI $\mathbf{T_{min}}$ is located over water. Second lowest T are found at tree surfaces
22:00	$\mathbf{T_{max}}$ located over tree surfaces and buildings → IUHI $\mathbf{T_{min}}$ located at open grass surfaces → Nocturnal PCI
03:00	$\mathbf{T_{max}}$ located over water surfaces. The second highest T is located over built up areas and tree surfaces → IUHI $\mathbf{T_{min}}$ located at open grass surfaces → Nocturnal PCI

Further on, a more specific overview for each night will be given. Note that the different figures (14, 16, 18 and 20) have different values presented in their legends, the maps are easier to compare vertically rather than horizontally. In figure 15, 17, 19 and 21 the temperature change (Δ T°C) of the 2004 LC and 2020 LC is presented and shows where the

highest and lowest temperature changes have occurred between the years. In table 8, 9, 10 and 11 the modeled wind speed and wind direction for the different nights is presented.

Night 25-26th

The night between the 25-26th has stable wind conditions with a consistent northerly direction and speed throughout the night. At 19:00 UTC the densely built-up area near the shore experiences lower temperatures compared to the built-up areas and grassland surfaces located further away from the shore, approximately 1-2 km. By 22:00 and 03:00 UTC, there is a shift, with these same built-up areas now experiencing some of the highest temperatures along with tree covered surfaces.

Table 8. *Modeled wind speed and wind direction during 25-26/7.*

UTC	**19:00**	**20:00**	**21:00**	**22:00**	**23:00**	**00:00**	**01:00**	**02:00**	**03:00**
Mod. WS (m/s)	2.5	2.5	2.7	2.9	3	3.1	3.1	3	2.9
Mod. W-Dir	N	N	N	N	N	N	N	N	N

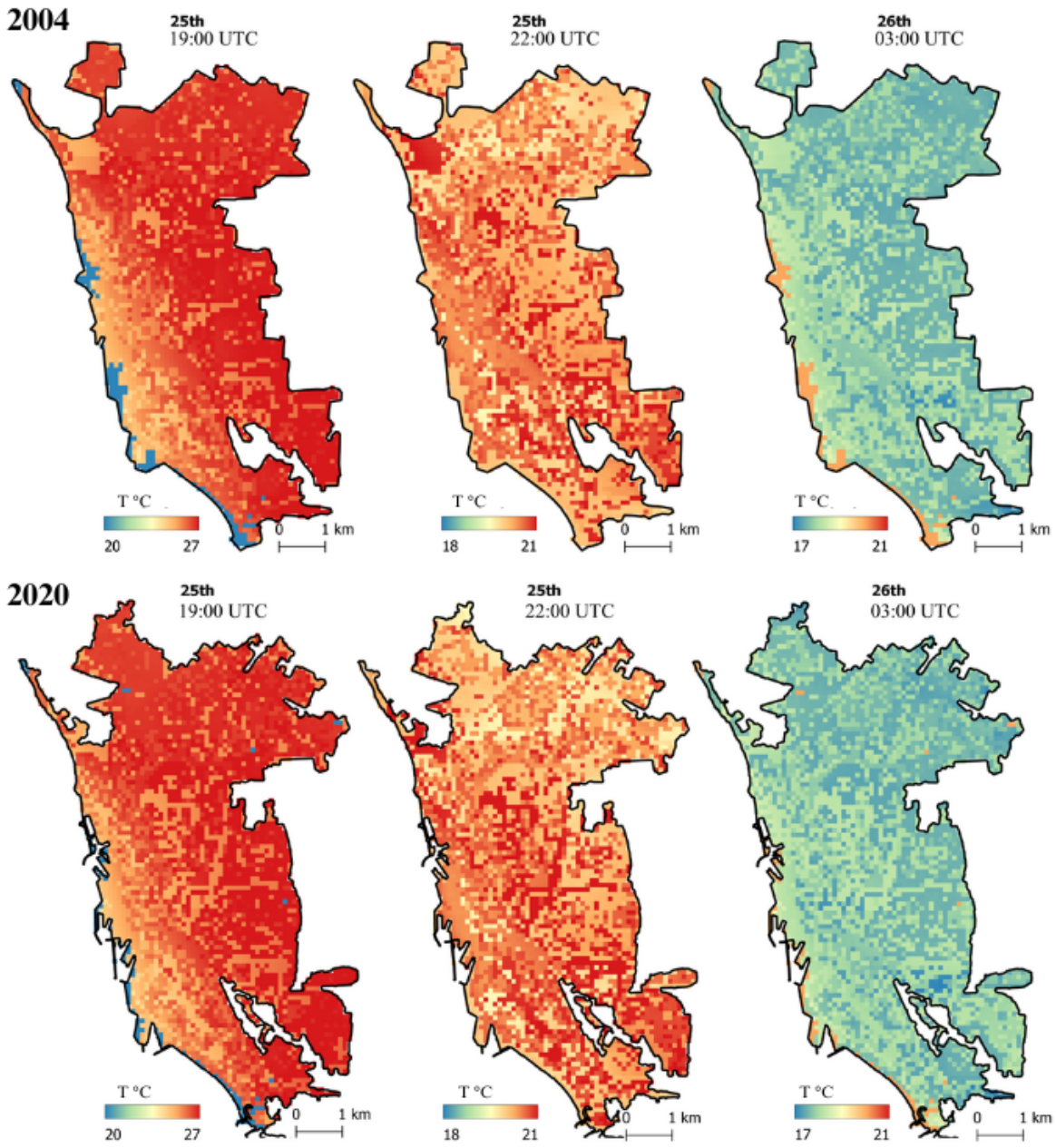

Figure 14 *presents the results from TAPM during the night of 25-26/7. Note the different values in the legends, comparison between the maps are easier done vertically rather than horizontally.*

In figure 15, the most significant ΔT°C are observed in areas where land cover has undergone changes over the years, especially in area A and B that were presented in figure 9, on page 25.

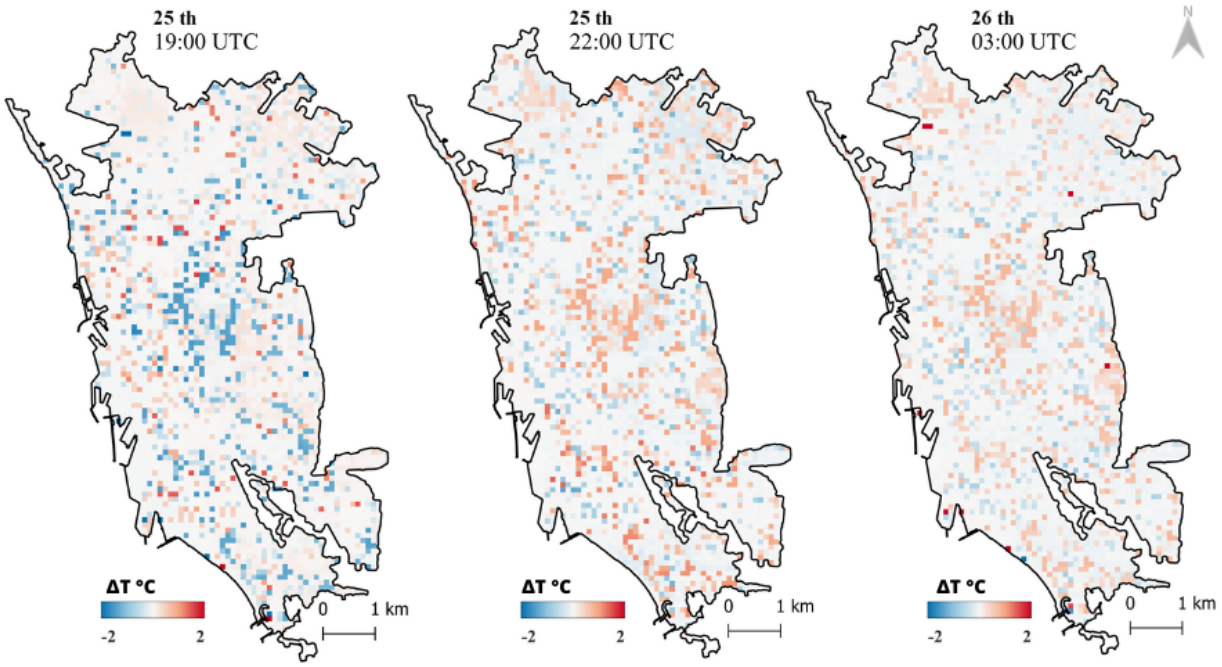

Figure 15. Mapping of Δ T°C at the three different times, between 2004 and 2020, on the night 25-26th.. Note that the temperature changes are related to the legend for each night and time presented in figure 14.

Night 26-27th

During the night 26-27th the modeled wind speed and direction varies. The wind speed is surpassing 3m/s at the start of the night and the direction shifts from northerly to easterly, see table 9. The highest temperatures are found closer to the city center, whereas the lowest temperatures are seen in the north east and south west at 22:00 and 03:00 UTC, possibly indicating influence from the wind, see figure 16.

Table 9. *Modeled wind speed and wind direction during 26-27/7.*

UTC	**19:00**	**20:00**	**21:00**	**22:00**	**23:00**	**00:00**	**01:00**	**02:00**	**03:00**
Mod. WS (m/s)	3.5	3.1	2.9	2.3	1.8	1.8	1.9	2	1.9
Mod. W-Dirr	N	N	NE	NE	E	E	E	E	E

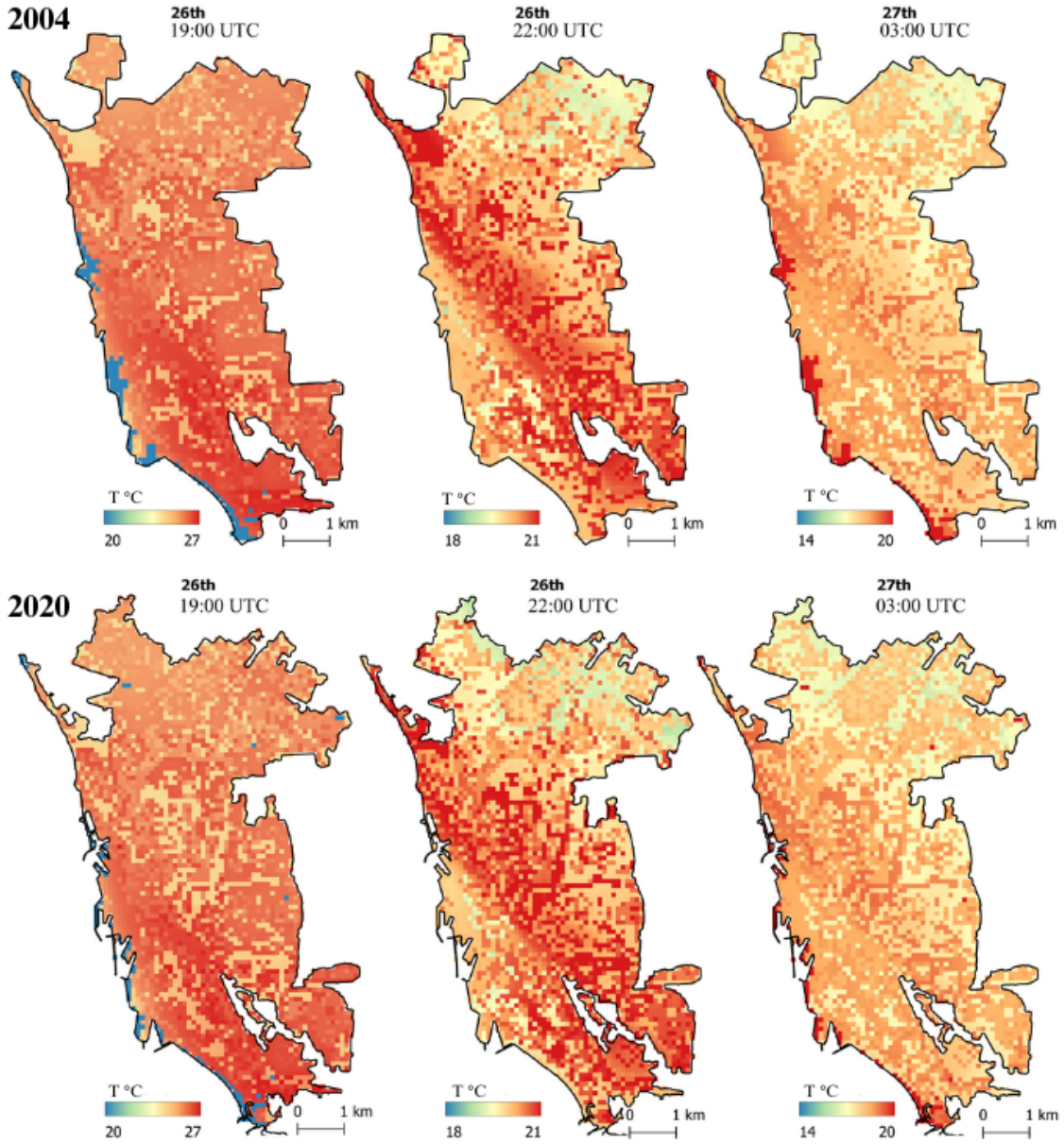

Figure 16*. Results from TAPM during the night of 26-27/7. Note the different range of the colorbar legends, comparison between the maps are easier done vertically rather than horizontally.*

In Figure 17, the most significant ΔT°C can be observed in areas where land cover has undergone changes over the years, particularly in area A and B as depicted in Figure 9 on page 25.

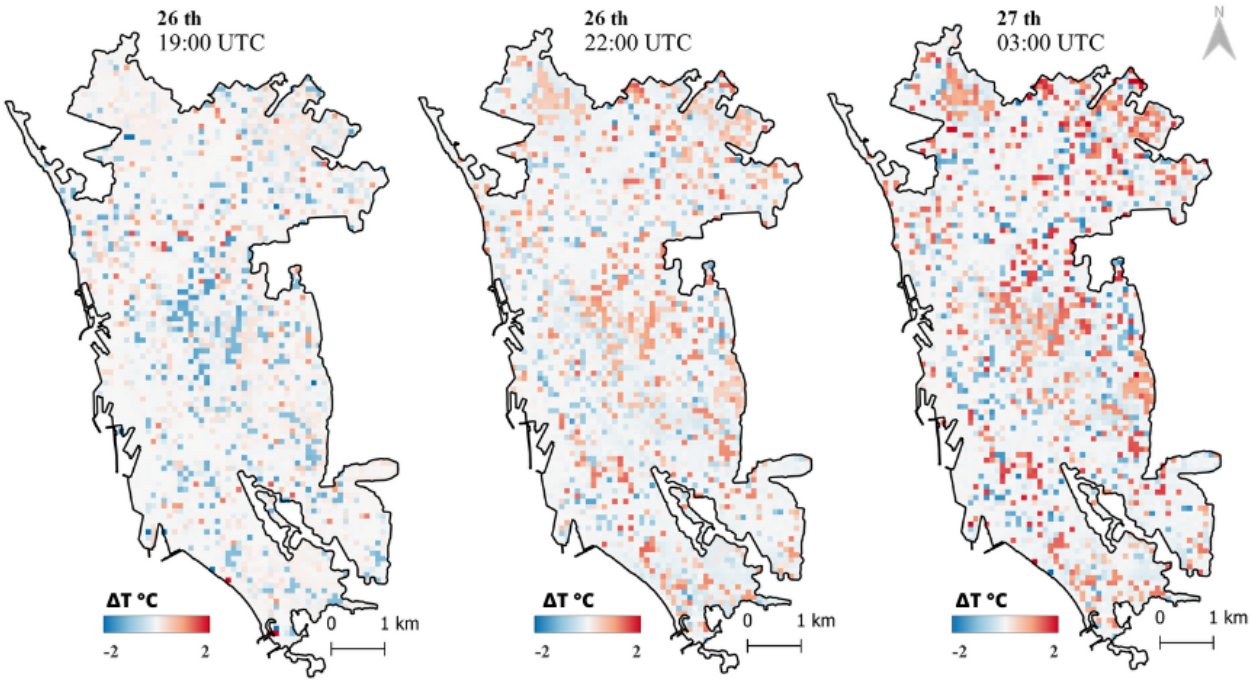

Figure 17. Mapping of Δ T°C at the three different times, between 2004 and 2020, on the night 26-27th.. Note that the temperature changes are related to the legend for each night and time presented in figure 16.

Night 27-28

The wind direction shifts during night and differs between each stroke, see table 10. In figure 18, notably, at 22:00, there is a change in wind direction, shifting from N (north) to NE (northeast). This change in wind direction may appear to impact the temperatures in the north eastern corner of the area. However, upon examining the maps at 22:00 UTC and comparing them to the maps at 03:00 UTC, a correlation between temperature patterns and wind direction can be observed. The higher temperatures appear to concentrate on the western side of the area, coinciding with the direction of the wind, and the city center.

Table 10. *Modeled wind speed and wind direction during 27-28/7.*

UTC	**19:00**	**20:00**	**21:00**	**22:00**	**23:00**	**00:00**	**01:00**	**02:00**	**03:00**
Mod. WS (m/s)	3.9	2.7	2.3	2.8	3.2	3.4	3.3	3.3	3.3
Mod. W-Dirr	E	E	E	NE	NE	NE	E	E	NE

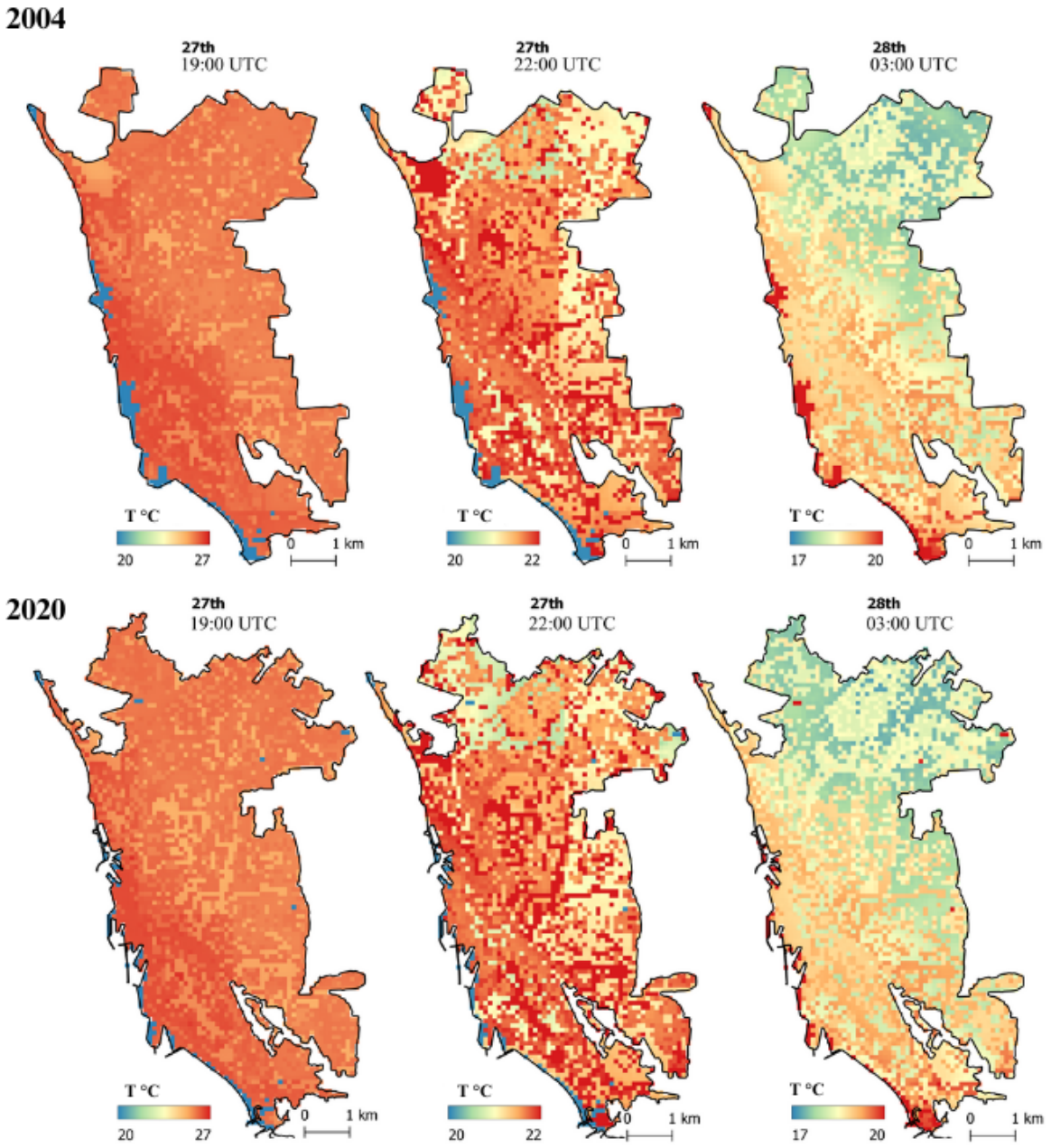

Figure 18*. Results from TAPM during the night of 27-28/7. Note that the maps have different legend values, comparison between the maps are easier done vertically rather than horizontally.*

In Figure 19, the most significant ΔT°C can be observed in areas where land cover has undergone changes over the years, particularly in area A and B as depicted in Figure 9 on page 25.

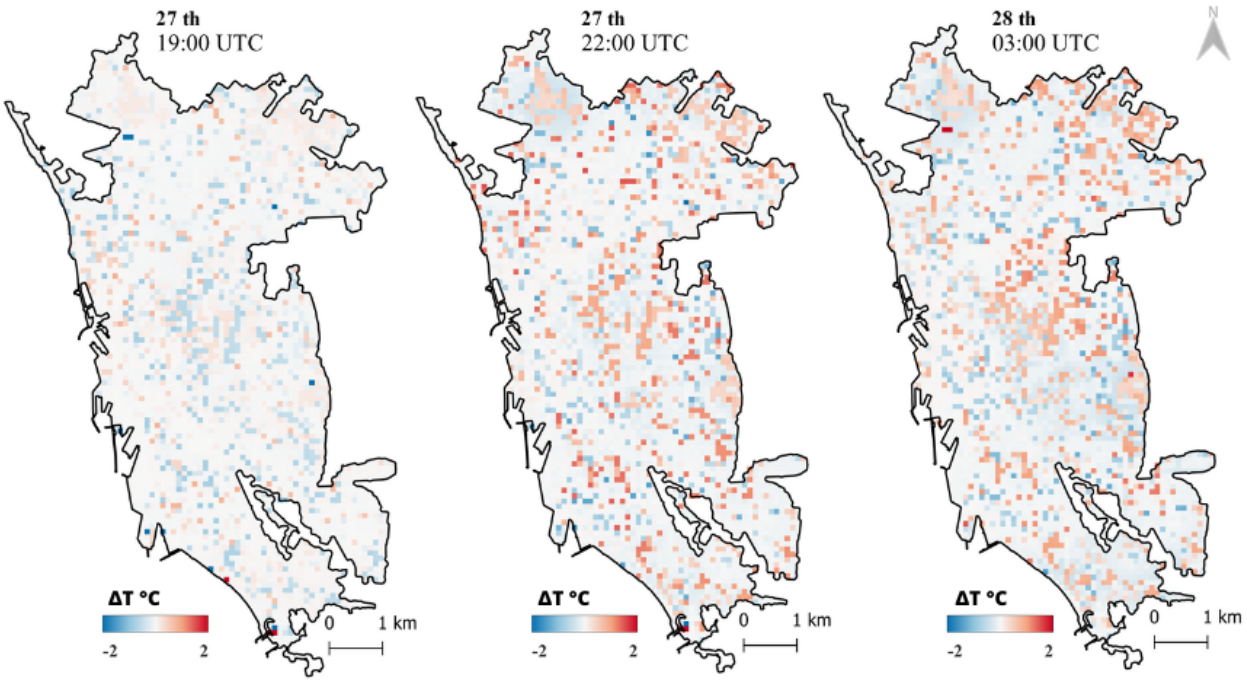

Figure 19. Mapping of Δ T°C at the three different times, between 2004 and 2020, on the night 27-28th.. Note that the temperature changes are related to the legend for each night and time presented in figure 18.

Night 29-30th

This night is the coldest of the modeled nights but shows a similar temperature pattern as previous nights. Low wind speeds and changing wind direction at each stroke. During 22:00 UTC a spot with much lower temperature can be found in the north-west corner, and may indicate a PCI. However, it is easier to distinguish between urban and vegetated surfaces during 03:00 as almost every vegetated surface obtains a value near $T_{min.}$.

Table 11. *Modeled wind speed and wind direction during 29-30th.*

UTC	**19:00**	**20:00**	**21:00**	**22:00**	**23:00**	**00:00**	**01:00**	**02:00**	**03:00**
Mod. WS (m/s)	1.7	1.6	1.5	1.6	1.5	1.7	1.6	1.9	2
Mod. W-Dir	N	NE	NE	E	E	E	SE	E	SE

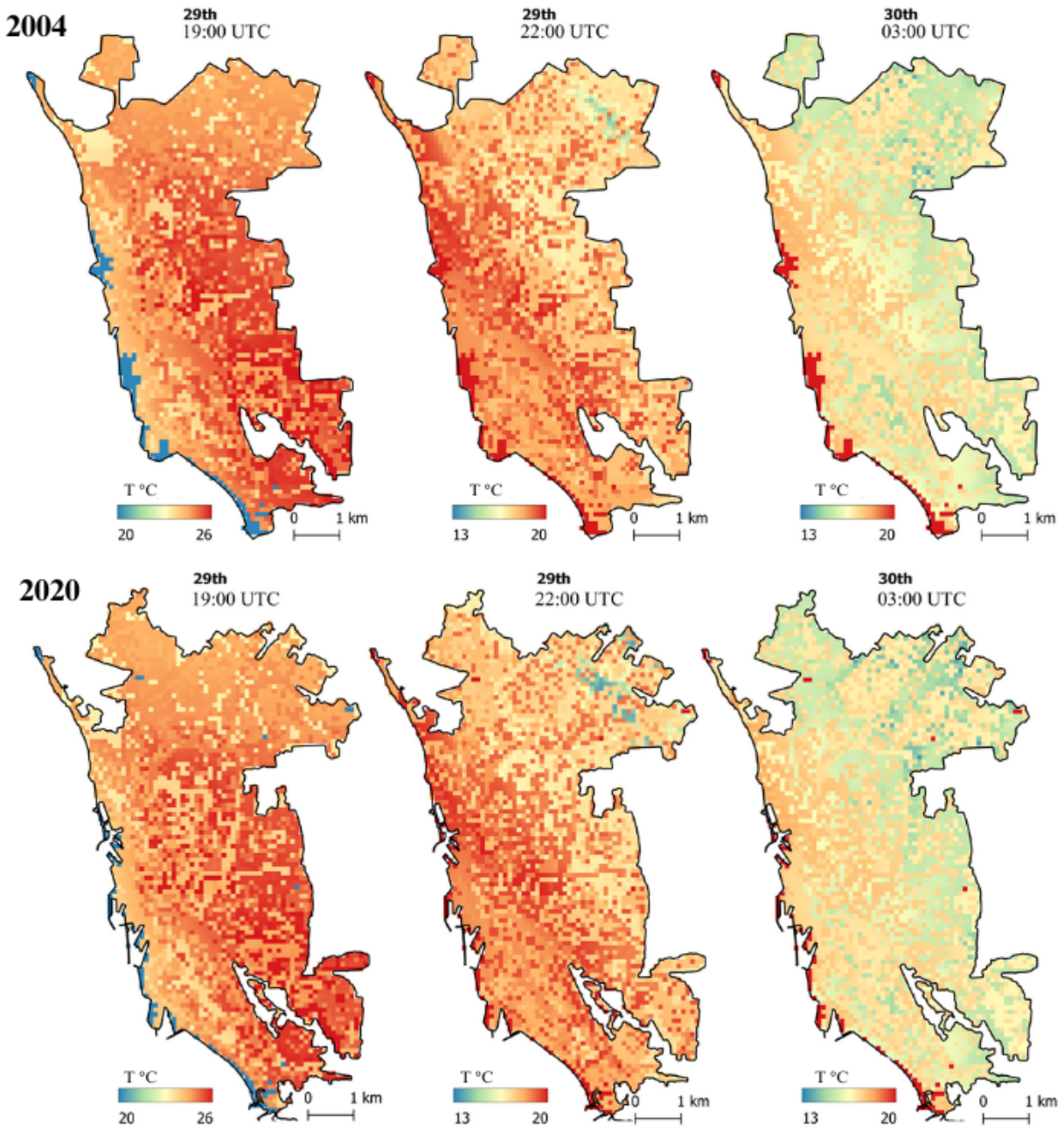

Figure 20. *Results from TAPM during the night of 28-29/7. Note that the maps have different legend values, comparison between the maps are easier done vertically rather than horizontally. .*

In figure 21, the most significant ΔT°C are observed in areas where land cover has undergone changes over the years, especially in area A and B that were presented in figure 9. Interestingly, despite being the coldest night, this specific night exhibits the most noticeable temperature difference between 2004 and 2020.

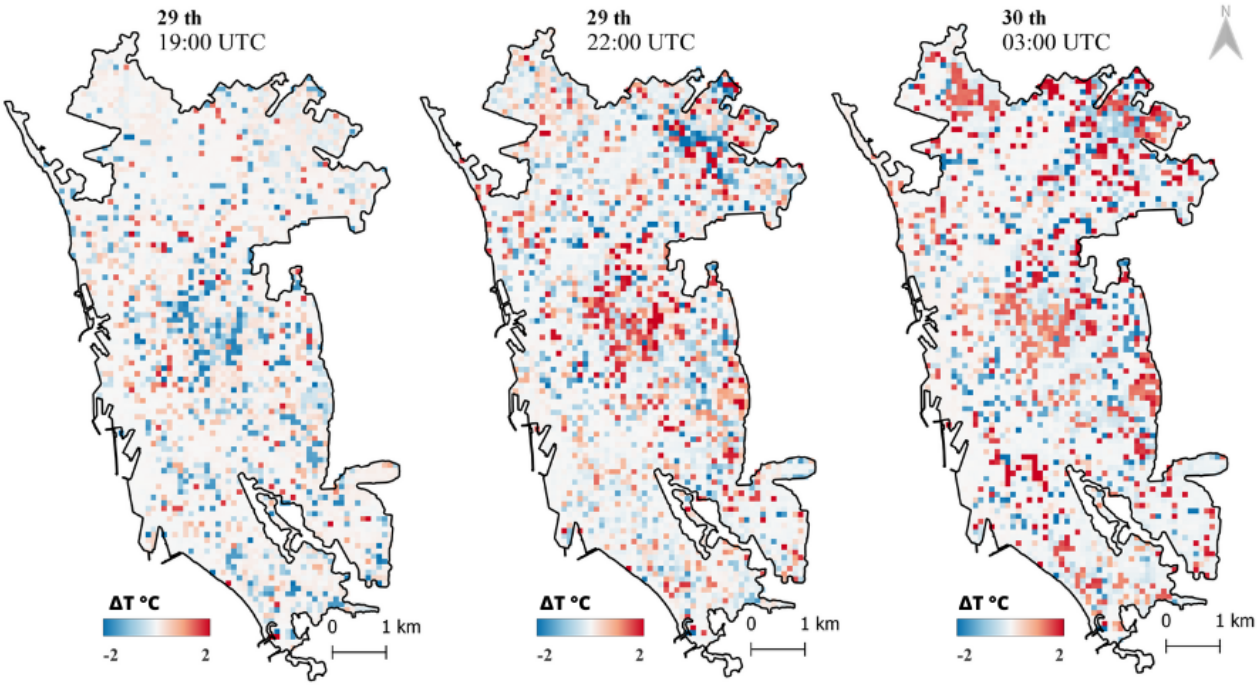

Figure 21. *Δ T°C during the night 29-30/7 , between 2020 and 2004. Note that the temperature changes are related to the legend for each night and time presented in figure 20.*

6.3.3 Mapping of high temperature distribution

To provide a comprehensive summary and comparative analysis of temperature patterns throughout the nights, as well as assess the magnitude of areas exposed to temperatures that pose a risk to human health (>18°C), the hour with the lowest temperature i.e 03:00 has been chosen as the reference point and visualized using a consistent legend and is shown in figure 18. None of the nights can be considered Tropic (>20°C) nor completely high (T_{min} >18°C), but there are still large areas that are at greater risk if a heatwave, like 2018, occurs again. This is especially shown during the 27th and 28th.

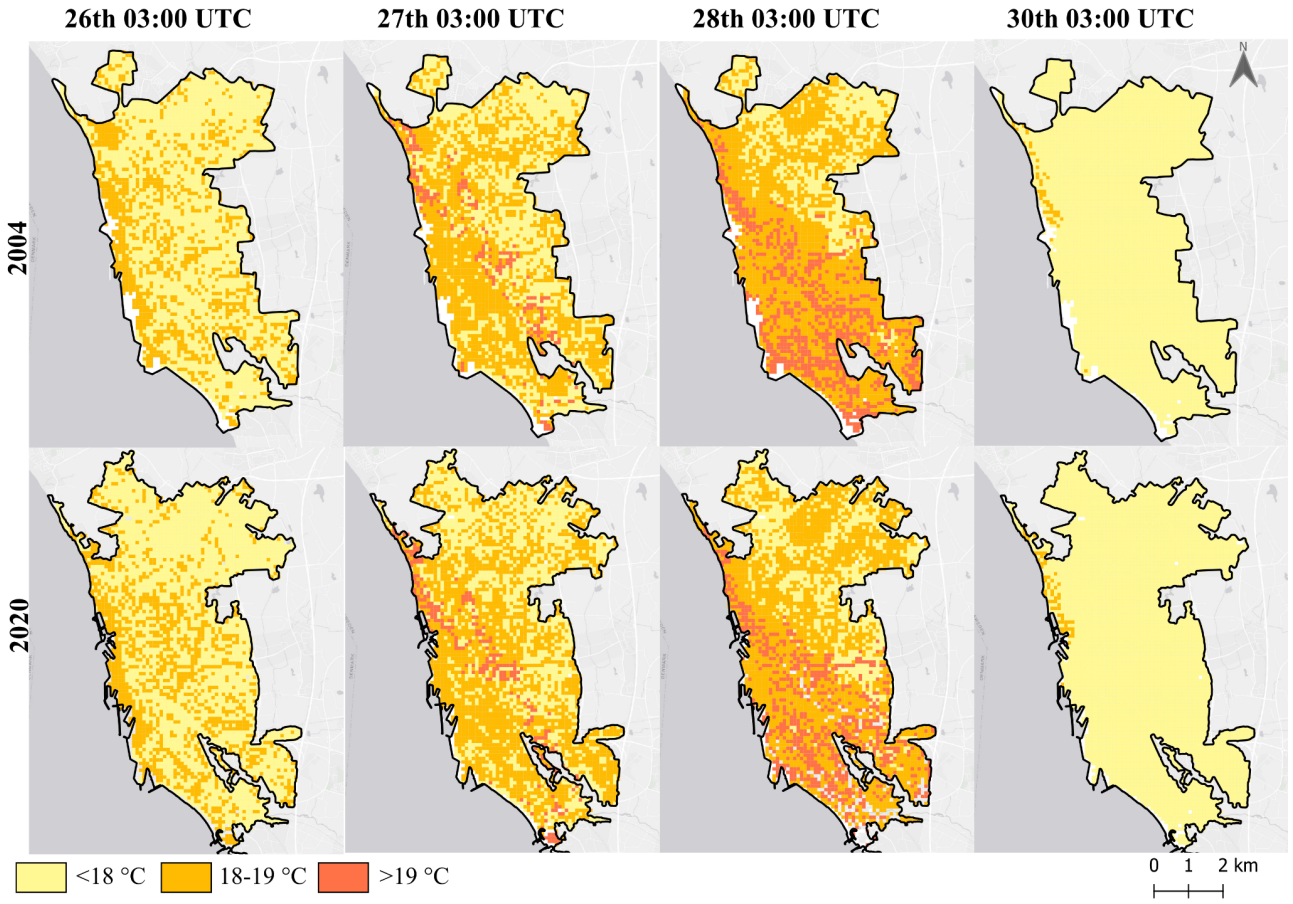

Figure 22. *Overview of the areas that have a temperature <18°C, 18-19°C or >19 °C during 03:00 for each night studied.*

Converting the mapped area into a bar plot demonstrates a decrease in the proportion of the total area with modeled temperatures <18°C from 2004 to 2020 for each analyzed night, accompanied by an increase in areas with temperatures >18°C (figure 22). It is important to note that no statistical test has been conducted, thus it remains undetermined whether there is a significant change in the modeled temperature distribution resulting from the land cover change

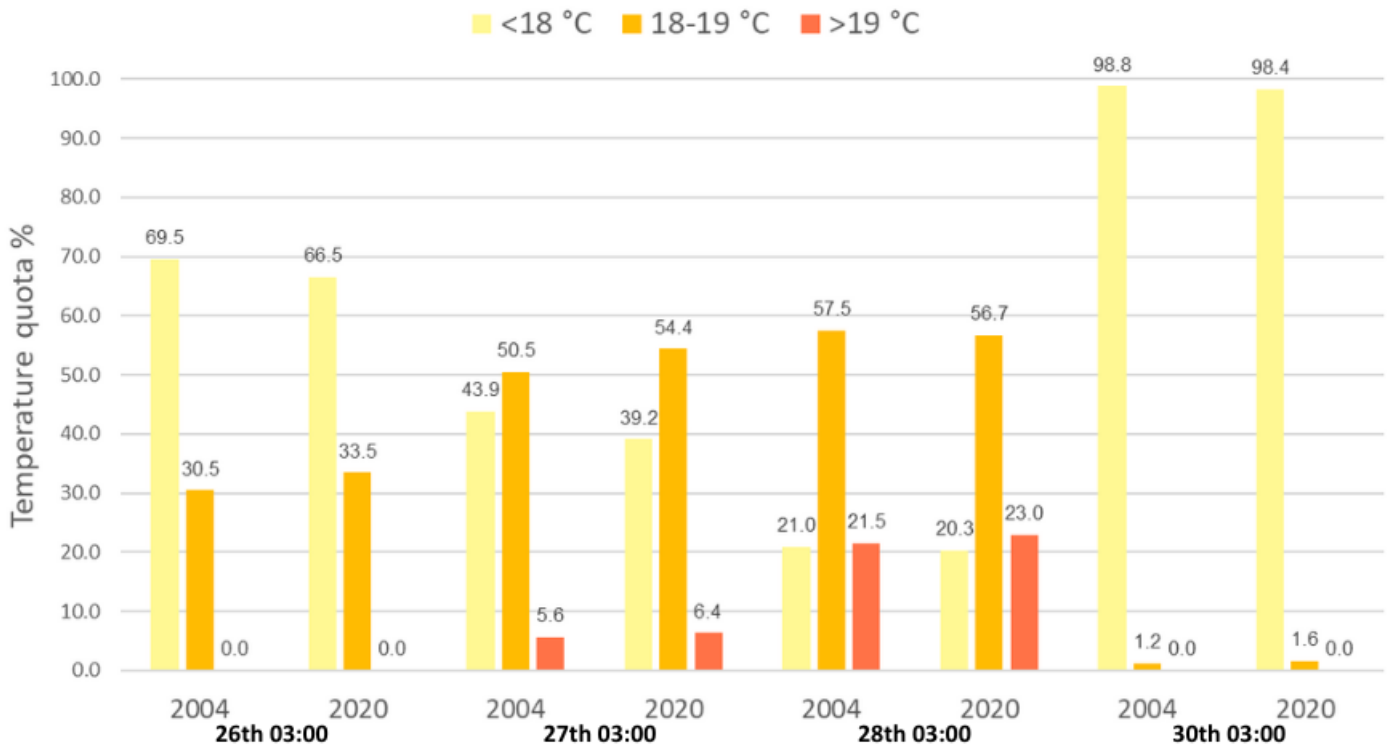

Figure 23. *Comparison of modeled temperature in % based on area during each night 2004 and 2020 at 03:00 UTC. Important to note is that the temperature is collected from the area where the two polygons of the study area (2004 and 2020) overlap.*

7. Discussion

Land Cover Changes in Helsingborg

The image classification indicates an increase in built up urban areas and an decrease in grass surfaces. Tree covered areas, on the other hand, have increased since 2004, this suggests a potential decline in grassland surfaces due to urbanization-induced land cover changes. Alternatively, it is possible that the growth of tree canopies has obscured the underlying grassland surfaces, considering the aerial perspective of the analysis. The increase in tree surfaces may imply an expansion of planted trees or wider canopies covering more areas. Remarkably, the HRLCC model exhibited a high overall accuracy of >90% in land cover classification, with few omission and commission errors. The high accuracy and confidence of this deep learning tool make it an useful resource for obtaining precise land cover information in future applications.

TAPM's ability to infer differences in Temperatures between different Land Covers

There are some indications that TAPM can infer differences in temperatures over different land covers. Seemingly easier to distinguish between vegetative and non-vegetated surfaces, during different times of the night. Thus, the overall result is that the six different LC-types used for this study have been difficult for TAPM to distinguish between all of them. For example during 19:00 UTC the general temperature pattern is that the lower temperatures are found at surfaces covered by trees and that T_{max} are found on open vegetated grassland and buildings. This makes it hard to distinguish between grassland (ID 18) and buildings (urban high ID 34 and urban low ID 32). During 22:00 the temperature starts to shift, during this time it gets easier to distinguish between grass surfaces and buildings. But since T_{max} are to be found at tree covered surfaces and built up areas it's hard to separate those two classes instead. During the coldest hour, 03:00 it gets even easier to extract grass surfaces but trees and buildings are still observed at somewhat the same temperatures. Without any comparing map or reference data it could therefore be hard to detect all different variations in the LC map.

With an R^2 of 0.91 between modeled and observed temperatures provides support for the reliability of the results. This indicates that the observed differences between the model output variability and the measured temperatures correlate well. In that sense this study confirms the findings that Chen M.D., et al (2002) did in their validation of TAPM on the

Swedish west coast whereby their study achieved an R2 of 0.92 for temperature and 0.60 for wind speed at a resolution of 1 km x 1 km. This study demonstrates that TAPM also produces favorable results at a higher resolution of 100 m x 100 m. On the other hand, just as in the study by Chen MD, et al (2002), the observed wind and modeled wind had a lower R^2 of 0.57, indicating a moderate correlation between the datasets.

The analysis of the modeled data suggests that TAPM has the potential to capture the influence of wind speed and wind direction on air temperature. As Yokobori and Ohta. (2009) stated wind is one of the most important variables affecting T which is why the model is advantageous as it considers factors beyond temperature and land cover and incorporates them in the modeling. Furthermore, this study demonstrates that it is possible to obtain high-resolution (100 x 100 m) assessments of air temperature at 2 meters, and that TAPM is also capable of capturing the intra-urban heat island effect (IUHI). Thus, it is important to note that this study only gathered data from one measuring station in Helsingborg, located outside of the city center located above a vegetated surface (see appendix 2), which may have affected the result. Nevertheless, the findings of this study demonstrate results that can be validated by other studies.

LCC's and the effect on nocturnal T

The overall findings from TAPM indicate that land cover changes have influenced temperature patterns, resulting in both increases and decreases depending on the time of night and the type of land cover. This is clearly observed in the Δ T maps, which highlight areas that have experienced temperature changes due to LCC's. The results suggest a general temperature shift in the study area, with a reduction in the occurrence of 100x100 pixel areas with temperatures <18 °C. However, it is important to note that this thesis lacks further statistical analysis to conclusively determine the extent and precise nature of these changes in reality.

Temperature variations were observed over areas where alterations in LC have occurred, but also in the general vicinity. This shows that Δ T are influenced by the changing land cover dynamics of the surrounding areas. The temperature pattern observed at 19:00 during the nights generally shows that areas with trees have lower temperatures compared to the

surrounding areas. This pattern may be indicative of the areas still being exposed to sunlight, with trees generating shadows or engaging in evapotranspiration, resulting in a cooling effect. On the other hand, during 22:00 and 03:00, some of the highest Δ T are found in tree covered areas. This finding aligns with the study conducted by Wujeska-Klause and Pfautsch (2020), which suggests that dense tree canopies can trap heat beneath the canopies during night. The general temperature pattern regarding grassland is that it possesses high T during sunlit conditions since the sun does not set yet for 20 min at 19:00 UTC. This aligns with Potcher, Cohen, and Bitan (2006) study saying that parks tend to be warmer than surrounding areas during sunlit conditions. This can also be a response to the settings in TAPM. Grassland possesses the highest stomatal resistance setting in TAPM at 150, which rules the amount of water vapor released from the vegetation during evapotranspiration, the higher the resistance the lower the water release. Which may be a result of why grassurfaces tend to be the warmest surfaces during 19:00 according to TAPM.

During 22:00 - 03:00 the intra urban temperatures change characteristics, whereas the areas with highest T are located over trees and the open grass surfaces are cooling off and obtains lower T then its surrounding, simulating Park cool Islands. Just as Spoken-Smith and Oke (1998) pointed out, open vegetated surfaces get colder than their surroundings during night. This phenomenon was captured every night. The coldest nights (29-30th) at 22:00 UTC and 03:00 UTC were most noticeable, even though it was the coldest of the investigated nights.

Despite 29th-30th being the coldest night it had the highest Δ T between the different nights. Since it could not be confirmed if this night had a cloud cover over 60% or not, and no precipitation data were modeled or observed during this night it was chosen to be used as a “normal temperature” night in Sweden. The high Δ T can indicate two things 1) the night actually has a cloud coverage and is trapping the radiation during night, affecting the Δ T. Or 2) it could be the fact that since TAPM is a dynamic model, it has stored heat from the earlier warmer days, which is released during the colder day.

The general differences between the years are of course correlated with LCC and the largest differences in temperature occur at the locations where “denser” LCC has been detected, which per say might not be a surprising result. To draw conclusions on why and how the temperature differs during the night together with LCC is not possible by just mapping the

areas and looking at differences between the different years (i.e different land covers), but it is important to try to validate the measured values with in situ measurements. The previously mentioned R^2 of 0.91 is based on data from one observational station during the period of 25-30th July 2018, and its corresponding modeled data. It would be necessary to have several observations, both from locations with and without LCC, to validate the model further on this 100x100m scale.

8. Further studies

Throughout the observed nights, no Southwestern wind was detected, suggesting that the results were not influenced by the wind from the sea. However, it is still possible to identify temperature patterns and areas with higher temperatures, which may be associated with wind direction and changes in land cover. This observation implies that TAPM may be capable of capturing the impact and movement of wind direction, thereby modeling temperature accordingly. However, this study alone is insufficient to confirm the validity of this theory. Therefore, further investigations are necessary to understand how TAPM accurately captures the influence of wind on air temperature.

In future research, it would be valuable to conduct experiments in TAPM involving a broader spectrum of land cover classes. This approach would enable the exploration of distinct classes that can be easily distinguished without compromising the credibility of the results. By examining a wider range of land cover types, researchers could gain deeper insights into their individual impacts on air temperature patterns. Additionally, it would be interesting to modify the land cover settings to incorporate different land cover classes and compare the resulting temperatures in those areas. This analysis would help understand how TAPM distinguishes between different land cover types and their corresponding temperature variations.

Additionally, it would be intriguing to expand the project's scope by extending the study period and considering different seasons. By analyzing temperature variations over an extended timeframe and in diverse climatic conditions, a more comprehensive understanding of the connections between land cover and air temperature could be established. This approach would provide a more nuanced perspective on how different land cover dynamics impact the urban microclimate and contribute to the formation of urban heat islands.

To explore the HRLCC model's capability for generating highly accurate land cover layers, it would be intriguing to apply the deep learning model using orthophotos of even higher resolutions, such as 0.16 or 0.5 meters, to assess if the model maintains high overall accuracy. Additionally, classifying more than 6 land cover classes would be interesting, as it could lead to the creation of more intricate and realistic maps, including the differentiation of various tree types.

9. Conclusions

In conclusion, the image classification results of Helsingborg in 2004 and 2020 using the deep learning model showed strong accuracy, demonstrating its effectiveness for remote sensing applications. The observed land cover changes indicate a decrease in grass areas and an increase in the proportion of trees. However, it is worth noting that the decrease in grass areas might be attributed to the presence of tree canopies covering the grass surface, leading to their exclusion from the classification.

TAPM demonstrates the ability to differentiate to some extent between different types of land cover, primarily distinguishing between vegetative and non-vegetative surfaces at different times during the night. It also generates satisfactory results at the local scale, allowing for the identification of distinct patterns. The modeled temperature data aligns well with the observed data at 2 m height. Although there is a slightly lower agreement in terms of wind at 10 m height, it is still considered acceptable. The observed land cover changes indicate a potential increase in areas experiencing high temperatures (>18 °C) in the event of similar heat waves to the one experienced in 2018. The presence of newly added trees appears to contribute to lower temperatures before sunset according to TAPM, but seems to have a warming effect during the night. Nonetheless, TAPM clearly demonstrates a nocturnal cooling pattern, with grass surfaces exhibiting the most significant cooling effect around midnight, Swedish local time, and shortly before sunset. Overall, these findings highlight the complex interactions between land cover, temperature, and wind patterns, emphasizing the need for further research and investigation to deepen the understanding of these dynamics and their implications in TAPM.

10. References

Articles/Books

Błażejczyk, K., Twardosz, R., Wałach, P. et al. *Heat strain and mortality effects of prolonged central European heat wave—an example of June 2019 in Poland.* Int J Biometeorol 66, 149–161 (2022). https://doi.org/10.1007/s00484-021-02202-0

Campbell, J. B., Wynne, R. H., & Thomas, V. A. (2022). Introduction to remote sensing. Guilford Publications.

Chen M.D., Wang T. Haeger-Eugensson M. Achberger C. Borne K (2002). *Application of TAPM (v.1) in Swedish West Coast: Validation during 1999-2000*. B2164. 2002. IVL: Swedish Environmental Research Institute.

Congalton, R.G. (1991). *A Review of Assessing the Accuracy of Classifications of Remotely Sensed Data*. Remote Sens. Environ.37:35-46 (1991). DOI: 10.1016/0034-4257(91)90048-B

Congalton RG and Green K. (2009). *Assessing the Accuracy of Remotely Sensed Data: Principles and Practices.* Second Edition. 2009 by Taylor & Francis Group, LLC

Copernicus (2022) Fraction of green vegetation cover. Collected 2023-05-15 from Fraction of green Vegetation Cover | Copernicus Global Land Service

Copernicus Climate Change Service, Climate Data Store, (2023): *ERA5 hourly data on single levels from 1940 to present.* Copernicus Climate Change Service (C3S) Climate Data Store (CDS), DOI: 10.24381/cds.adbb2d47 (Accessed on 11-05-2023)

de Blij, H. J.,Muller, O. P., Burt, J.E & Mason, J.A. (2013). Physical Geography. Oxford University press. Fourth Edition.

Good, E.J. (2016). *An in situ-based analysis of the relationship between land surface"skin"and screen-level air temperatures*. ,J. Geophys. Res. Atmos.,121, 8801–8819, doi:10.1002/2016JD025318

Hart, M.A., Sailor, D.J. *Quantifying the influence of land-use and surface characteristics on spatial variability in the urban heat island.* Theor Appl Climatol 95, 397–406 (2009). https://doi-org.ezproxy.ub.gu.se/10.1007/s00704-008-0017-5

Hersbach, H., Bell, B., Berrisford, P., Biavati, G., Horholmeránvi, A., Muñoz Sabater, J., Nicolas, J., Peubey, C., Radu, R., Rozum, I., Schepers, D., Simmons, A., Soci, C., Dee, D., Thépaut, J-N. (2023): ERA5 hourly data on pressure levels from 1940 to present. Copernicus Climate

Holmer, B. Thorsson, S. Eliasson, I. (2007). *Cooling rates, sky view factors and the development of intra‐urban air temperature differences*, Geografiska Annaler: Series A, Physical Geography, 89:4, 237-248, DOI: 10.1111/j.1468-0459.2007.00323.x.

Huang, K. Li, X, Liu X. and K. C. Seto. *Projecting global urban land expansion and heat island intensification through 2050*, Environ. Res. Lett., vol. 14, no. 11, 2019

Hurley, P. (2008). *TAPM. v4. Part 1: Technical Description*. CSIRO Marine and Atmospheric Reasearch Paper. No. 25. 2008. ISBN: 978-1-921424-71-7. ISSN: ISSN: 1835-1476.

IPCC. 2022. *Climate Change 2022: Impacts, Adaptation and Vulnerability.* Contribution of Working Group II to the Sixth Assessment Report of the Intergovernmental Panel on Climate Change [H.-O. Pörtner, D.C. Roberts, M. Tignor, E.S. Poloczanska, K. Mintenbeck, A. Alegría, M. Craig, S. Langsdorf, S. Löschke, V. Möller, A. Okem, B. Rama (eds.)]. Cambridge University Press

Konarska et al. (2016). *Influence of vegetation and building geometry on the spatial variations of air temperature and cooling rates in a high-latitude city*. Int. J. Climatol. 36: 2379–2395 (2016). doi: 10.1002/joc.4502

Lan, Y and Zhan, Q. (2017). *How do urban buildings impact summer air temperature? The effect of building configurations in space and time.* Science Direct. Volume 125, 2017. pages 88-89. https://doi.org/10.1016/j.buildenv.2017.08.046

Lillesand, Thomas M., Ralph W. Kiefer, and Jonathan W. Chipman. *Remote Sensing and Image Interpretation*. 7.th ed. 2015. Print.

Liu Yiqing et al. (2022). *Revising the definition of anthropogenic heat flux from buildings: role of human activities and building storage heat flux*. EGU.2022. doi: https://doi.org/10.5194/acp-22-4721-2022

Mahmood, R. et al (2013). *Land Cover Changes and their biophysical effects on climate*. International Journal of Climatology, Volume 34. DOI number: https://doi-org.ezproxy.ub.gu.se/10.1002/joc.3736

Majeed H, Floras JS *Warmer summer nocturnal surface air temperatures and cardiovascular disease death risk: a population-based study.* BMJ Open 2022;12:e056806. doi: 10.1136/bmjopen-2021-056806

Mohan, Giridhar, M.V.S.S. (2022). *A Brief Review of Recent Developments in the integration of Deep Learning with GIS*. Geomatics and environmental engineering. Volume 16. Number 2. 2022. doi: https://doi.org/10.7494/geom.2022.16.2.21

Monteith, J. L., Szeicz, G., & Waggoner, P. E. (1965). *The Measurement and Control of Stomatal Resistance in the Field.* Journal of Applied Ecology, 2(2), 345–355. https://doi.org/10.2307/2401484

Onomura, S. Holmer, B. Lindberg, F. and Thorsson, S. (2016). *Inta-urban nocturnal cooling rates: development and evaluation of the NOCRA model*. Volume 23, Issue 3. doi: https://doi.org/10.1002/met.1558.

Vulova, S. Meier, F. Fenner, D. Nouri, H. and Kleinschmit, B. "*Summer Nights in Berlin, Germany: Modeling Air Temperature Spatially With Remote Sensing, Crowdsourced Weather Data, and Machine Learning*," in IEEE Journal of Selected Topics in Applied Earth Observations and Remote Sensing, vol. 13, pp. 5074-5087, 2020, doi: 10.1109/JSTARS.2020.3019696

Savage, M.J. (2016) *Nowcasting daily minimum air and grass temperature*. Int J Biometeorol 60, 183–194 . https://doi-org.ezproxy.ub.gu.se/10.1007/s00484-015-1017-7

Spronken-Smith and Oke. (1998). *The thermal regime of urban parks in two cities with different summer climates.* INT. J. Remote Sensing, 1998, Vol. 19. NO 11, 2085-2104. https://doi-org.ezproxy.ub.gu.se/10.1080/014311698214884

Thorsson, S. et al. (2014). Mean Radiant Temperature - A predictor of heat related mortality. Science Direct. Urban Climate. Volume 10, Part 2. doi: doi.org/10.1016/j.uclim.2014.01.004

Tomczyk AM. (2018). *Impact of Atmospheric Circulation on the Occurrence of Hot Nights in Central Europe*. Atmosphere. 2018; 9(12):474. https://doi.org/10.3390/atmos9120474

Wujeska-Klause A, Pfautsch S. (2020). *The Best Urban Trees for Daytime Cooling Leave Nights Slightly Warmer*. Forests. 2020; 11(9):945. https://doi.org/10.3390/f11090945

Yokobori, T and Ohta, S. (2009). *Effect of land cover on air temperatures involved in the development of an intra-urban heat island.* Climate Research. Vol 39: 61-73. 2009. DOI: 10.3354/cr00800

Zipper et al. (2016). *Urban heat island impacts on phenelogy: intra-urban variability and response to land cover.* Environmental Research letters 11. doi:10.1088/1748-9326/11/5/054023
Creating individual zones with Region Group—ArcGIS Pro | Documentation

Websites

Esri (n.d) ArcGIS pretrained models - *High Resolution Land Cover Classification - USA*. Collected 2023-05-07 from: https://doc.arcgis.com/en/pretrained-models/latest/imagery/introduction-to-high-resolution-land-cover-classification-usa.htm

Esri (2021a) Accuracy Assessment for image classification (Image Analyst). ArcMap. collected 2023-03-01 from: Accuracy Assessment for image classification (Image Analyst)—ArcMap| Documentation (arcgis.com)

Esri (2021b) Create Accuracy Assessment Points (Spatial Analyst). ArcMap. collected 2023-05-07 from: Create Accuracy Assessment Points (Spatial Analyst)—ArcMap | Documentation (arcgis.com)

Swedish Public Health Agency (2022). Swe. Folkhälsomyndigheten (2022). *Hälsoeffekter av värmeböljor – En kunskapssammanställning.* Artikelnummer: 22084. Collected 2023-05-17 from: Hälsoeffekter av värmeböljor – En kunskapssammanställning — Folkhälsomyndigheten (folkhalsomyndigheten.se)

Fondriest (2010) *What is Air Temperature?* Collected 2023-03-02 from: https://www.fondriest.com/news/airtemperature.htm

Helsingborg (2022) Collected 2023-03-10 from: https://helsingborg.se/kommun-och-politik/statistik/befolkningsutveckling-och-folkmangd/

SCB (2022) Collected 2023-03-10 from: https://www.scb.se/hitta-statistik/sverige-i-siffror/miljo/tatorter-i-sverige/

SMHI (2011). Klimatanalys för Skåne Län. Rapport nr 2011-52. Microsoft Word-SMHI-#134803-Klimatanalys_för_Skåne_län_slutversion (lansstyrelsen.se)

SMHI (2018) *Sommaren 2018*. Collected 2023-05-11 from Sommaren 2018 - Extremt varm och solig | SMHI https://www.smhi.se/polopoly_fs/1.165089!/Klimatologi_52%20Sommaren%202018%20-%20en%20glimt%20av%20framtiden.pdf

SMHI (n.d. a) *Hur var vädret då?* - Helsingborg. Collected 2023-05-07. from Hur var vädret? - Helsingborg (smhi.se)

SMHI (n.d. b). *Senaste Observationer Vatten*. Collected 2023-04-10 from SMHI - Observationer Sverige | SMHI

SMHI (n.d. c). *Senaste Observationer Väder.* Collected 2023-04-10 from SMHI - Observationer Sverige | SMHI

United Nations (2020) Population Facts 2020/2: *Policies on spatial distribution and urbanization have broad impacts on sustainable development.* Collected: 2023-04-05 https://www.un.org/development/desa/pd/sites/www.un.org.development.desa.pd/files/undes_pd_2020_popfacts_urbanization_policies.pdf

World population review (n.d) Collected 2023-04-10 from: https://worldpopulationreview.com/ - world population

11. Appendices

Appendix 1

Accuracy assessment

> *"A classification is not complete until its accuracy is assessed"* (Lillesand et al., 2015)

In any classification project, evaluating an *accuracy assessment* is a crucial step that involves comparing the classified image with a reliable data source known as *ground truth* or *reference data.* Ground truth is the actual land cover type present on the ground and its information can either be collected in the field or be determined manually in GIS using high resolution data (Esri, 2021a). Important to note is that "ground truth" usually is based on the reference data but even though the reference data is considered to be correct, the data may not be perfect or represent the real "truth" (Congalton .R.G,. Green. K. 2009). One way of determining the classified value and the ground truth is to create reference points/sample units that enable the analyst to compare the classification and the ground truth at the same location. This can be done using one of the three sampling methods: *Random, Stratified Random or equalized Stratified Random* (Esri, 2021b).

> ***Random*** *- Distribution of random points within an image, does not take classification categories into consideration.*
>
> ***Stratified Random*** *- Points get randomly distributed, within each classification category, whereas each classification category gets a set of points in relation to its relative area.*
>
> ***Equalized Stratified Random*** *- Points get randomly distributed within each classification category, where each category gets the same number of points.*

Confusion Matrix

One of the most effective ways to determine a classified image's accuracy is to compute an *error matrix*, also called *confusion matrix* (Congalton .R.G,. Green. K. 2009 ; Lillesand et al., 2015). The purpose of a confusion matrix is to "…*determine how well a classification has categorized a representative set of test pixels whose true classes were determined by the ground truth data"* (Lillesand et al., 2015). The matrix compares the ground truth and the results from a classification, by the help of sample units, and consists of equal amounts of columns and rows as there are categories whose classification accuracy is being assessed. As a rule of thumb, according to Congalton .R.G,. Green. K. (2009) and Lillesand et al (2015) there should be a minimum of 50 sample units for each class if the area of observation is

covering less than a million acres (4046,8 km2). Larger areas or if more then 12 classes are being used a higher number of samples, 75-100, is required. Congalton, R.G (1991) also points out that the amount of samples per category can be adjusted based on the importance of the category for the desired mapping. Sometimes it is better to concentrate the sampling units on the categories of interest and increase the sampling units for those categories and reduce the number of samples for categories with no/low importance for the mapping (ibid).

Sample units that have been correctly classified are presented in the matrix's diagonal line (upper left to lower right), see table 1. Samples that have been wrongfully classified are presented in the horizontal and vertical lines, excluding the values included in the diagonal line (Lillesand et al 2015). A confusion matrix presents the accuracy of each category, including any errors of inclusion (*commission errors*) and exclusion (*omission errors*) that may have occurred during classification. A commission error refers to the inclusion of an area in a category that it does not belong to, while an omission error refers to the exclusion of an area from the category which it actually belongs to (Congalton .R.G,. Green. K. 2009).

Table 1 *shows an example on a confusion matrix and its variables. The matrix is a made up one to explain the concept of it, the values are therefore not related to analysis in this study.*

LC Type	**Water**	**Forest**	**Bare soil**	**Urban**	**Total**	**UA**	**Kappa**
Water	**100**	0	0	0	100	100%	0
Forest	0	**237**	2	21	260	91%	0
Bare Soil	0	0	**48**	2	50	96%	0
Urban	0	35	5	**160**	200	80%	0
Total	100	272	55	183	**610**	0	0
PA	100%	87%	87%	87%	0	***OA 89%***	0
Kappa	0	0	0	0	0	0	**71%**

The purpose of a confusion matrix extends beyond showcasing error measures for individual classes; it also provides an assessment of the Overall accuracy (OA). OA represents the overall percentage of accurately classified classes (Congalton .R.G,. Green. K. 2009). The overall accuracy in table 1 is 89%, this is calculated using *Equation 1* (ibid):

$$OA = \frac{\sum_{i=1}^{r} x_{ii}}{N}$$

Equation 1

where

r = total number of rows (classes) in the confusion matrix

x_{ii} *= total number of correctly classified pixel observations for each class*

N = total number of pixel observations in the confusion matrix (610 in table 1)

An universal agreement is that an overall accuracy should be ≥ 85% for the classification to be considered sufficient and to be used in further analysis (Congalton .R.G., Green. K. 2009; Lillesand et al,. 2015). According to Congalton R.G. and Green. K. (2009) there is no direct explanation to why that value was adopted and that in some applications an OA of 85% is considered to be more than sufficient while others argue that an OA should be higher.

In table 1 there are variables called UA, PA and Kappa, these stands for *Users Accuracy*, *Producer's Accuracy* and *Kappacoefficient* (K). PA and UA shows the accuracies and errors for each individual category. The producer's accuracy is calculated column wise, by dividing the total number of correct classified sample units by the total number of sample units indicated by the ground truth data (Congalton .R.G,. Green. K.,2009). The producer's accuracy explains how well the sampling units for each category have been classified while the user's accuracy tells us the probability that a pixel classified into a category actually represents the ground truth (Lillesand. et al,. 2015).

Performing a *Kappa analysis* is a useful approach when comparing two confusion matrices with each other. *K* provides an indication of the *true agreement* between the remotely sensed classification and the ground truth by taking *chance agreement* into account, i.e. the scenario where sample units have been classified correctly by chance rather than correct modeling. The coefficient ranges between 0 and 1 (or 0 to 100%), where 0 indicates chance agreement and 1 indicates true agreement, which is ideal. In cases where chance agreement is large (closer to 0 than 1), *K* indicates that there has been a poor classification performance. To calculate K, *Equation 2* is used (Lillesand et al,. 2015):

$$\kappa = \frac{N \sum_{i=1}^{r} x_{ii} - \sum_{i=1}^{r} (x_{i+} \cdot x_{+i})}{N^2 - \sum_{i=1}^{r} (x_{i+} \cdot x_{+i})}$$

Equation 2

where

r = total number of rows (classes) in the confusion matrix

xii = total number of correctly classified pixel observations for each class

N = total number of pixel observations in the confusion matrix (610 in table 1)

Xi+ = total number of pixel observations of the modeled classification for each class

x+i = total number of pixel observations of the test data of each class

Appendix 2

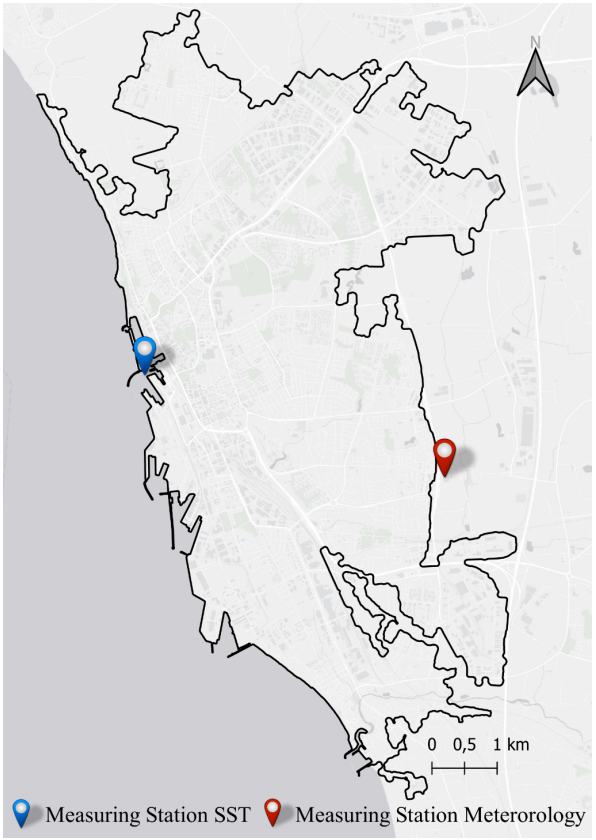

The location of SMHIs measurement stations. The meteorological station is located outside of the urban area, above vegetated surfaces,43,7 m.a.s.l. Source: SMHI (n.d a and b).

Appendix 3

The different available types of vegetation and their variables in TAPM. Source: Hurley. P,. 2008

Vegetation Types:	h_f (m)	σ_f	LAI	r_{si} (m^{-1})
-1: Permanent snow/ice	-	-	-	-
0: Water	-	-	-	-
1: Forest – tall dense	42.00	0.75	4.8	370
2: Forest – tall mid-dense	36.50	0.75	6.3	330
3: Forest – dense	25.00	0.75	5.0	260
4: Forest – mid-dense	17.00	0.50	3.8	200
5: Forest – sparse (woodland)	12.00	0.25	2.8	150
6: Forest – very sparse (woodland)	10.00	0.25	2.5	130
7: Forest – low dense	9.00	0.75	3.9	200
8: Forest – low mid-dense	7.00	0.50	2.8	150
9: Forest – low sparse (woodland)	5.50	0.25	2.0	110
10: Shrub-land – tall mid-dense (scrub)	3.00	0.50	2.6	160
11: Shrub-land – tall sparse	2.50	0.25	1.7	100
12: Shrub-land – tall very sparse	2.00	0.25	1.9	120
13: Shrub-land – low mid-dense	1.00	0.50	1.4	90
14: Shrub-land – low sparse	0.60	0.25	1.5	90
15: Shrub-land – low very sparse	0.50	0.25	1.2	80
16: Grassland – sparse hummock	0.50	0.25	1.6	90
17: Grassland – very sparse hummock	0.45	0.25	1.4	90
18: Grassland – dense tussock	0.75	0.75	2.3	150
19: Grassland – mid-dense tussock	0.60	0.50	1.2	80
20: Grassland – sparse tussock	0.45	0.25	1.7	100
21: Grassland – very sparse tussock	0.40	0.25	1.2	80
22: Pasture/herb-field – dense (perennial)	0.60	0.75	2.3	80
23: Pasture/herb-field – dense (seasonal)	0.60	0.75	2.3	80
24: Pasture/herb-field – mid-dense (perennial)	0.45	0.50	1.2	40
25: Pasture/herb-field – mid-dense (seasonal)	0.45	0.50	1.2	40
26: Pasture/herb-field – sparse	0.35	0.25	1.9	120
27: Pasture/herb-field – very sparse	0.30	0.25	1.0	80
28: Littoral	2.50	0.50	3.0	180
29: Permanent lake	-	-	-	-
30: Ephemeral lake (salt)	-	-	-	-
31: Urban	10.00	0.75	2.0	100
32: Urban (low)	8.00	0.75	2.0	100
33: Urban (medium)	12.00	0.75	2.0	100
34: Urban (high)	16.00	0.75	2.0	100
35: Urban (cbd)	20.00	0.75	2.0	100
36: Industrial (low)	10.00	0.75	2.0	100
37: Industrial (medium)	10.00	0.75	2.0	100
38: Industrial (high)	10.00	0.75	2.0	100

The urban and industrial land use characteristics that are used in TAPM. Source: Hurley, P. 2008.

Land-use Types:	σ_U	α_U	A_U	k_U	z_{oU}
31: Urban	0.50	0.15	30	4.6	1.0
32: Urban (low)	0.50	0.17	20	1.5	0.4
33: Urban (medium)	0.65	0.15	30	5.0	0.6
34: Urban (high)	0.80	0.13	40	8.0	0.8
35: Urban (cbd)	0.95	0.10	70	10.0	2.0
36: Industrial (low)	0.50	0.15	50	4.6	0.5
37: Industrial (medium)	0.65	0.15	100	4.6	1.0
38: Industrial (high)	0.80	0.15	150	4.6	1.5